HELSINKI UNIVERSITY OF TECHNOLOGY
Department of Electronics

Juha Sälli

Implementation of residual current protection in photovoltaic inverters

Helsinki, 9.11.2009

Supervisor: Professor Raimo Sepponen

Instructor: Master of Science Mikko Paakkinen

HELSINKI UNIVERSITY OF TECHNOLOGY		ABSTRACT OF THE MASTER'S THESIS	
Author	Juha Timo Olavi Sälli		
Title of the thesis	Implementation of residual current protection in photovoltaic inverters		
Date	9.11.2009	Number of pages	88
Department	Department of Electronics		
Professorship	S-66		
Supervisor	Professor Raimo Sepponen		
Instructor	Master of Science Mikko Paakkinen		

The number of photovoltaic systems in distributed energy production is increasing rapidly, one advantage being pollution free energy production. Residual currents are, however, something that can disturb the operation of these systems. Residual currents are caused by the ground capacitance of the solar panels and the voltage created across this capacitance. All the choices made in the design of the system affect these problematic residual currents. The design choices include modulation technique, inverter topology and used solar panel type. Residual currents result in higher losses, fire hazard as well as risk of electric shock. Standards regulate the permitted residual currents. One of these standards is VDE DIN 0126-1-1 which permits maximum residual current of 300 mA. Fast 30 mA changes have to be detected immediately.

The causes and effects of residual current are studied in this thesis which concentrates on systems feeding the grid using transformerless inverters. The thesis examines methods to measure residual currents. Two commercial residual current sensors are tested and compared. Following this comparison, a prototype sensor is designed, simulated and built. Tests are performed in order to obtain more insight into the practical issues affecting residual current measuring. Fluxgate was chosen as the technology used in the prototype sensor.

The commercial sensors tested operated as documented, but clear differences could be found in their operation. The prototype sensor was built successfully and it was able to measure residual currents as required by the standards. However, the prototype sensor was particularly sensitive to external magnetic fields. The shielding of the measuring device should be studied more in future development.

Keywords: photovoltaic, residual current. flux gate, ground capacitance,

inverter

TEKNILLINEN KORKEAKOULU		**DIPLOMITYÖN TIIVISTELMÄ**	
Tekijä	Juha Timo Olavi Sälli		
Työn nimi	Vikavirtasuojauksen toteuttaminen aurinkoinverttereissä		
Päivämäärä	27.10.2009	Sivumäärä	88
Osasto	Department of Electronics		
Professuuri	S-66		
Työn valvoja	Professori Raimo Sepponen		
Työn ohjaaja	Diplomi-insinööri Mikko Paakkinen		

Aurinkosähköjärjestelmien käyttö hajautetussa energiantuotannossa lisääntyy voimakkaasti. Aurinkosähköjärjestelmien etuna on mm. päästötön energiantuotanto. Vikavirrat voivat häiritä näiden järjestelmien toimintaa. Vikavirrat aiheutuvat aurinkopaneelin maakapasitanssista ja tämän yli muodostuneesta jännitteestä. Kaikki järjestelmässä tehdyt valinnat vaikuttavat syntyviin vikavirtoihin. Näitä valintoja ovat mm. modulaatiotekniikka, käytetty invertteritopologia ja aurinkopaneelityyppi. Vikavirrat aiheuttavat järjestelmässä mm. kasvaneita häviöitä, tulipalovaaran ja sähköiskun vaaran. Standardit määrittelevät rajat sallituille vikavirroille. Esimerkiksi VDE DIN 0126-1-1 [12] määrittelee suurimmaksi sallituksi vikavirraksi 300 mA. Nopeat 30 mA muutokset tulee huomata välittömästi.

Tässä työssä tutkittiin vikavirtojen syntyä ja vaikutuksia verkkoon syöttävissä järjestelmissä jotka käyttävät muuntajattomia inverttereitä. Myös vikavirran mittaustapoja tutkittiin. Kahta kaupallista vikavirtasensoria testattiin ja niitä vertailtiin keskenään. Työssä suunniteltiin, simuloitiin ja rakennettiin oma prototyyppisensori. Tällä tavoin tutustuttiin tarkemmin vikavirtamittaukseen ja sen toimintaan käytännössä. Prototyyppisensorin teknologiaksi valittiin flux gate tekniikka.

Testatut kaupalliset sensorit toimivat dokumentoidulla tavalla. Niiden toiminnassa oli kumminkin selviä eroja. Prototyyppisensori saatiin toimimaan ja sillä voitiin mitata standardien vaatimia virtoja. Sensori oli hyvin herkkä ulkopuolisille magneettikentille ja suojautumista näiltä kentiltä tulee tutkia tarkemmin tulevaisuudessa.

Avainsanoja: aurinkosähkö, vikavirta, flux gate, maakapasitanssi, invertteri

Foreword

It's always a pleasure to work with nice people and study an interesting subject. Best is when you have both and I was lucky to have those two. I'd like to thank my instructor Mikko Paakkinen for guidance and good feedback. Also, thanks to my professor Raimo Sepponen. I'd also like to thank Matti Jussila for tips you gave me along the way. William Martin gave me guidance in the linguistic form of the thesis and deserves many thanks.

Special thanks to my family and little sister who raced me in graduation. I still think it's only fair that I graduated before you because I'm the Big'Brou. I'm sorry that we didn't make that bet on "who's first" ;)

Rock on Rockers!

Helsinki, 23.10.2009

Juha Sälli

Table of Contents

Abbreviations and symbols

Abbreviations

1206	Package type of SMD components
3E27	Ferromagnetic core material
AC	Alternating current
BAV99	Package type of SMD diodes
CH	Oscilloscope channel
DC	Direct current
DC-AC	Device inverting direct current to alternating current
DC-DC	Device changing direct current voltage level
DIN	German national organization for standardization (in German: Deutsches Institut für Normung).
DRV401	Current measuring IC, manufacturer Texas Instruments
EMI	Electromagnetic interference
EN	Organization to foster the European economy in global trading (European Committee for Standardization)
FMEA	Failure mode and effects analysis
IC	Integrated circuit
IEC	International Electrotechnical Commission (International standardization organization)
Na^+	Natrium ion
PV	Photovoltaic
PWM	Pulse width modulation
/PWM	Inverted pulse width modulation signal
QFN-20	Quad Flat No leads, SMD IC package
RC-filter	Filter consisting of resistors and capacitors
RCMU	Residual current monitoring unit
RMS	Root mean square
SQUID	Superconducting quantum interference device
SO-20	Small-outline package for SMD IC
SOT-23	Small-outline package for SMD transistors and diodes

VDE	German Association for Electrical, Electronic and Information Technologies (in German: Verband der Elektrotechnik, Elektronik und Informationstechnik)

Symbols

A	Area
b_a	Total inside length of the U-core limb containing the air gap
B, B_0	Magnetic flux density
$B_{u\text{-}core\_pri}$	Magnetic flux density induced by primary current
B_r	Remanent magnetization
B_{sat}	Saturated magnetic flux density
B_{toroid}	Magnetic flux density inside a toroid
d	Coil length, distance
di/dt	Rate of current change
dl	Differential length
dv/dt	Rate of voltage change
E	Energy
f, f_0	Frequency
F	Force
G	Gain
GND	Ground
H	Magnetic field strength
H_c	Magnetic field coersity
H_{comp_coil}	Magnetic field strength induced by compensation coil to compensation core
H_{comp_pri}	Magnetic field strength induced by primary current to compensation core
H_{gap_comp}	Magnetic field strength induced by compensation coil to air gap
H_{gap_pri}	Magnetic field strength induced by primary current to air gap

H_{ex_pri}	Magnetic field strength induced by primary current to excitation core
I	Current
I_{comp}	Compensation current
I_{pri}	Primary current
k	Sensing factor
kW_p	Peak power generation capability of the system
l_e	Effective length
$l_{e,u\text{-}core}$	Effective length of a compensation core consisting of two U-cores
$l_{e,toroid}$	Effective length of a toroid structure
l_g	Length of an air gap
L	inductance
N	Number of turns
P	Power
q	charge
r	Radius of a circle
r_{eff}	Effective radius
R	Resistance
R_{osc}	Resistance of oscilloscope
S	Area
U	Voltage
U_{out}	Output voltage
μ	Permeability
μ_0	Permeability of the vacuum
μ_r	Relative permeability
μ_e	Effective permeability
$\mu_{e,toroid}$	Effective permeability of a toroid
$\mu_{e,u\text{-}core}$	Effective permeability of a U-core
μ_c	Permeability of a core
v	Charge carrier velocity
v_{ind}	Voltage induced to coil
V	Volume

V_C	Supply voltage
+ V_{CC}	Positive supply voltage
- V_{CC}	Negative supply voltage
V_{DC}	DC voltage of the inverter
V_h	Hall voltage
$V_{p\text{-}p}$	Peek to peek voltage

1 Introduction

Distributed power production utilizing solar energy is on the increase. In 2008, the capacity of new photovoltaic (PV) system installations increased globally by 110 % to 5.95 gigawatts [1]. The advantages of photovoltaic energy are pollution free power production utilizing a ubiquitous and free energy source, the sun. Furthermore, photovoltaic energy can be produced almost anywhere. It is used in satellites orbiting the earth as well as on earth in large power plants which produce tens of megawatts. Photovoltaic systems consist of solar-panels, an inverter, support structures and low voltage equipment like overvoltage protection and relays. An inverter is needed to convert the DC-current of the solar-panels to the AC-current needed by consumers. The inverter also manages possible failures in the system such as loss of the grid as well as excessive residual currents. Residual currents cause numerous adverse effects on the photovoltaic system and its users. The residual currents generated in the grid feeding photovoltaic systems are regulated by standards. One important standard is the German VDE DIN 0126-1-1 [12]. It requires the residual currents to be measured in the range of 30 mA to 300 mA.

The work done in this thesis was divided into four major tasks. The first task was to benchmark and verify the operation of the residual current measurement devices for a photovoltaic inverter. Devices from two manufacturers were tested. The devices have to fulfill the requirements of VDE DIN 0126-1-1 standard. The second task was to obtain a general view of the solutions available to measure residual currents, the criteria for a good solution being cost efficiency and smallness in size. The third task was to study the creation mechanisms of the residual currents in grid feeding PV-systems using transformerless inverters. The effects of the residual currents were studied as well. The fourth and final task was to build a prototype sensor for residual current monitoring based on the most suitable technology and to verify it’s operation.

The background of photovoltaic energy production is presented in the second chapter. Also, the causes and effects of residual currents are studied in the second chapter. The third chapter deals with the measuring principles of the residual current and various technologies applied in measuring. The fourth chapter takes a look at the commercial solutions available on the markets and tests two devices. Measurements are made to find the differences in the offers of the two manufacturers. In the fifth chapter the prototype sensor is designed and built. In the sixth chapter the prototype sensor is tested. A summary of the thesis is presented in the seventh and last chapter.

2 Background

A solar panel is the basic building block of the photovoltaic power system. Solar panels consist of a series connected solar cells which are essentially diodes utilizing the photovoltaic effect. In the photovoltaic effect, matter emits electrons when it has absorbed energy from photons of electromagnetic radiation. The kinetic energy of the absorbed photon has to be equal to or more than the minimum energy required to remove an electron. The kinetic energy of a photon is proportional to the wavelength of it. The wavelength of the radiation has to be less than the material specific threshold wavelength for the matter to emit electrons. Higher intensity levels do not accelerate the emission of electrons if the wavelength is too high [29]. Solar cells have to be manufactured from appropriate materials so that the photons in sunlight can knock electrons loose in the cells. Silicon, for example, is a suitable and widely used material for solar-cells. The loose electrons are only allowed to move in one direction creating a usable DC-current. Photovoltaic inverters are used to convert the DC-current into the required voltage and frequency.

The first modern solar cells were manufactured from silicon that was doped with certain impurities in the late fifties. The efficiency was poor, only about 6 percent. Since then, newer technologies and materials like Gallium arsenide have been introduced in manufacturing. Modern cells can achieve a maximum efficiency of over 40 percent in laboratories where the sunlight is concentrated hundreds of times [43]. Material costs are of critical importance in mass production and many of the cells use a considerable amount of energy and material in production. Thin-film cells are promising due to their low energy and material costs. The efficiency of thin-film cells is around 5,5 % to 7,0 % while thicker crystalline silicon cells have a typical efficiency of 11,9 % to 13,1 % [30].

PV-arrays connected to the inverter are constructed linking tens of PV-modules together. PV-modules are further compiled from tens of smaller solar cells. The inverter converts the DC-current from the PV-arrays into the

required AC-current. The AC-current can then be fed to the public grid or to an isolated local grid. The inverter is responsible for failure situations and safe operation during the failure. The support structures for PV-arrays and the inverter can also be included in the system. Low voltage equipment in the system consists of connectors and safety functions such as overvoltage protections, relays and fuses.

Photovoltaic inverters can be divided roughly into two categories: transformerless inverters and inverters with a transformer. Transformers generally reduce the efficiency of the inverters and increase the weight and expenses. Transformerless inverters in comparison are more efficient, cheaper, smaller in size and are lighter in weight. Their structure is simpler compared to inverters with a transformer [2]. Some national grid codes still require inverters to have a transformer because transformers make galvanic separation between the grid and the PV-arrays. The separation of the grid and the PV-arrays is a safety measure. The separated PV-panels are in a different potential compared to the grid grounded support structures. This decreases the possibility of electric shock hazard because the residual current will not flow directly between the grid ground and the PV-arrays. It is also feared that in the transformerless systems DC-side faults could be conducted directly to the AC-grid causing serious problems in the public grid [26]. Inverters with transformers also have negligible leakage currents.

Inverters containing transformer can be further divided into two sub categories. Low frequency transformers, also called line transformers, are placed between the inverter stage and the grid. Line transformers are operated at the grid frequency which is 50 Hz in Europe. Furthermore, line transformers are large in size and heavy in weight. Their cost is also an issue. An inverter using a line transformer has to be controlled and driven in such a way that the line transformer is not saturated. High frequency transformers are smaller than low frequency transformers and are placed between the panels and the inverter stage. Usually the high frequency transformers operate in the frequency range of 10 kHz to 50 kHz. The

inverter using a high frequency transformer has to be controlled in such a way that no DC-component is created in the current fed to the grid. The driving circuitry is more complex in inverters with high frequency transformers than in inverters with low frequency transformers [2].

The lack of galvanic separation in transformerless inverters could lead to higher residual currents depending on the setup in question. The residual currents result from capacitance between the ground and the cells of the photovoltaic modules and the potential difference across this capacitance [2]. Residual currents have many adverse effects as discussed in section 2.3. Residual currents, DC-injection and human safety can be controlled with monitoring systems, converter control strategies and other technologies. All requirements set in the modern standards are meant to improve the safety of the inverters.

2.1 Terminology

Various terms are used when discussing residual currents. Typically terms like residual current, ground current, leakage current, fault current and earth current are used. They all refer to the common mode current. These currents are measured with the same methods. The term residual current will be used in this text.

Leakage currents are created when currents flow through the stray capacitances. The part of the main current that does not return the normal path is called the residual current. The earth fault current is a current that is generated due to an insulation fault, which can be between any live part and ground. Earth fault currents are abnormal and the system has to shut down if an earth fault occurs. Some level of leakage current exists always in real systems. Leakage currents are normal and they are allowed within some limits.

2.2 Residual currents in solar systems

A ground capacitance is formed between the photovoltaic cells and the grounded frame of the cell. A voltage is created across the ground capacitance and it creates a current through the capacitance depending on the frequency of the amplitude of the voltage. The current is common mode. All parts of the photovoltaic system interact with the residual currents; panels, installation place, grounding, inverter and the grid. Moreover, weather conditions have to be kept in mind.

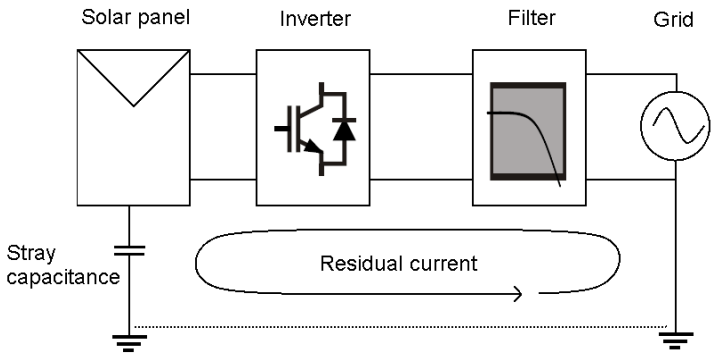

Figure 1: Residual current path

The modulation method used in the inverter is the most dominant factor in residual currents [39]. Two widely used modulation methods exist; bipolar and unipolar. The bipolar modulation method uses two voltage levels, $+V_{DC}$ and $-V_{DC}$, to invert the DC-current into AC-current. The voltage created across the ground capacitance in a standard full bridge photovoltaic inverter is half of the voltage of the grid and it is in the grid frequency [38]. The residual currents are minimal in the bipolar modulation because the grid frequency is very low, only 50 Hz in Europe. The unipolar modulation method uses three voltage levels in operation, $+V_{DC}$, 0 and $-V_{DC}$. The main disadvantage is that a high frequency voltage component is created across the ground capacitance in the standard full bridge photovoltaic inverter. The high frequency voltage sees the ground capacitance as a low impedance path and creates high residual currents through it. The unipolar modulation method, however, has several advantages when compared to the bipolar

modulation. The switching frequency of the inverter can be lowered to half of the bipolar modulation switching frequency while still keeping the same effective switching output frequency. The voltage across the filter inductors change by V_{DC} during each switching, while in bipolar switching it is $2xV_{DC.}$ This means a decreased *dv/dt* and a lower ripple current. The unipolar modulation method decrease switching losses, EMI-emissions and filtering requirements [38].

Panel types have an impact on residual currents. The ground capacitance between the cell and grounded frame is the characteristic of the panel affecting the residual currents. The older generation crystalline silicon cells typically have capacitances from 50 to 150 nF/kW_p. On the other hand, newer thin-film cells can have capacitances up to 1 $\mu F/kW_p$ [37].

The voltage created across the ground capacitance depends also on the topology used in DC-AC-stage and, possibly, the DC-DC-stage. The standard full bridge photovoltaic inverter typically creates some voltage across the ground capacitance. Some topologies are able to eliminate the voltage across the ground capacitance. Neutral point clamped inverter topology, for example, has no residual currents through the ground capacitance [38], making it a very interesting topology.

Weather has a crucial role in residual currents. Humidity and the temperature of the air being the two key factors which increase residual currents. Residual current uses three main paths in the PV-modules [36]. The first is from the cell through the top cover glass to the surface of the glass. From there the current flows on the surface to the grounded frame. The second path is straight from the cell to the frame via the glass. This occurs near the frame. The third path is from the cell to the frame through the insulation between the cell and frame. The second and the third paths are both high impedance paths and they are dominant under dry conditions. The first path is the

dominant leakage current path in more humid conditions. The condensing humidity creates a low impedance path on top of the cover glass. The resulting increase in residual current is enormous as presented in reference [36]. The module measured was biased to -600 V and at clear noon with relative humidity of 12,8 % the residual currents were 92 nA. During a cloudy night the relative humidity increased to 87,4 %. The residual currents increased accordingly to 1742 nA. Concurrently temperature decreased from 39,1 °C to 19,6 °C.

2.3 Effects of residual currents

Residual currents have many adverse effects on the whole photovoltaic system and its users, the most severe effect being the risk of electric shock for human beings. This might occur when the residual current flows via the parasitic capacitances of the panels to system parts that are not meant to be energized. The high AC-voltage in the energized parts causes shock hazard when a person connected to ground touches these system parts. The energy from the part discharges through the person to the ground.

The other severe risk is fire hazard. The current leaking from the photovoltaic system can flow through parts that heat and catch fire or ignite material next to it. Building integrated panels are grounded to the building structure and the residual currents flow through this structure which is usually partly metallic [4]. The place of fire hazard or human being exposed to electric shock can be separate from the panels themselves.

Moreover, residual currents accelerate the degradation process of the photovoltaic panels. The residual current between the cell and the metallic frame are directly comparable to the damage in the panels. The degradation process depends strongly on the polarity of the voltage applied to the panels [6]. It has been proposed that the Na^+-ions from the front glass react with the

materials used in the panels. Water might accelerate the reaction because the process is faster under humid conditions [5][6].

Radiated and conducted electromagnetic interference (EMI) is increased due to residual currents. The parasitic capacitance of the panel provides an additional path for the high frequency currents to flow out of the system and interfere with other devices. Residual currents increase the general losses in the inverter and add harmonics and otherwise distort the current fed into the grid [2][7][8]. Voltage fluctuations in panels also create electric and magnetic fields around them which increase the EMI problems.[11]

Excessive residual currents might saturate the common mode chokes of EMI-filters. Electromagnetic emission levels will rise if the chokes saturate [9][10]. Also, voltage spikes and high levels of ripple coming through the filters might either damage or shut down the system.

2.4 Standards

Standards determine the technical requirements that photovoltaic inverters have to fulfill and the methods that are used to test the requirements. At the moment international standards lag behind the current progress of photovoltaic systems. Many of the standards are still drafts and work is still to be done to publish them officially. Every country can have their own regulations regarding photovoltaic systems. This thesis concentrates on two standards. One of them is international standard and the other is a German national standard which is taken into consideration because it is the most comprehensive standard in the field of solar electricity. The German photovoltaic markets are also the second largest in the world so the pressure for a valid standard is high.

In the USA transformerless inverters cannot be used because of national regulations. A transformer is needed to achieve galvanic isolation between the grid and the solar panels. This thesis will not discuss the issues in the USA any further. The standard dealing with the issues in the USA is UL508C "Power Conversion Equipment" [42].

2.4.1 VDE DIN 0126-1-1

VDE DIN 0126-1-1 "*Selbsttätige Schaltstelle zwischen einer netzparallelen Eigenerzeugungsanlage und dem öffentlichen Niederspannungsnetz*" is a standard from the German standardization organization DIN [12]. It covers automatic disconnection between the generator and the public grid. According to VDE DIN 0126-1-1, residual currents should never be greater than 300 mA. In case of residual currents higher than 300 mA, the system should shut-off in 0.3 seconds. For rapid changes in residual current the standard permits the limits shown in Table 1. Sudden changes are monitored because they might occur when a human touches energized parts of the system.

Table 1: VDE limits for residual current

Current (mA)	Shut-off time (s)
30	0.3
60	0.15
150	0.04

The standard requires the residual current monitoring unit (RCMU) to be able to monitor DC, impulse and AC fault currents. Moreover, the standard limits the monitored frequency range to 2 kHz and below. The current values are RMS-values [12].

2.4.2 IEC 62109-2

IEC 62109-2 "*safety of power converters for use in photovoltaic power systems – Particular requirements for inverters*" is a standard from the IEC (International Electrotechnical Commission) [41]. The Standard defines safety and power quality requirements for stand-alone and grid connected inverters.

The standard assigns a limit to the residual current according to the peak power generation capability of the system. The maximum residual current allowed is 60 mA/kW_p. For rapid changes, the current and shut-off time limits are as in Table 1 describing the VDE limits. The RCMU has to be of type B. Type B is defined in the IEC standard 60755 "*General requirements for residual current operated protective devices*" [40]. The B type RCMU detects the following residual current types whether suddenly applied or slowly rising:

- Sinusoidal residual currents up to 1 kHz
- Pulsating direct residual currents
- Smooth direct residual currents
- Previous types combined together
- Direct residual currents resulted from rectifying circuits, referring to known residual current pulse types described in standard 60755

3 Methods of residual current measurement

By nature residual currents are common mode currents. A common mode current appears to travel on both, phase and neutral lines of the inverter. The return path is the common ground (See Figure 1). The main current of the system is a differential mode current that uses phase-line to travel and neutral-line to return.

Only Hall sensor and fluxgate methods were chosen to be further studied in this chapter. They are widely available commercially and their price range is acceptable, offering lossless measurement and the size of the devices is suitable. Many other means also exist to measure currents. Methods like optical current measuring, giant magnetoresistance, SQUID (Superconducting Quantum Interference Device) and search-coil-sensors can be used to measure current but they all have some major drawbacks most commonly cost and size.

3.1 Measurement problem description

The standards provide the guidelines for measuring residual current. Residual current devices have to be able to measure all residual current components in photovoltaic inverters. The device has to be capable of measuring AC-, DC-, and pulsating DC residual currents as well as combination of these all. The device has to be capable of recognizing 30 mA changes and it has to measure residual currents at least up to 300 mA according to the VDE standard.

Currents in general can be measured with a shunt resistor in series with the main conductor. The current *I* flowing through the known resistance *R* can be measured from the voltage *U* created across the resistance. Equation (1) presents Ohm's law.

$$U = RI \Leftrightarrow I = \frac{U}{R} \quad \textbf{(1)}$$

The resistance should be low so that the losses created in the resistance would also be low. A resistor is usually chosen so that with the maximum current of the voltage reading is dozens of millivolts. Resistive measuring is the most linear method of measuring current and it is accurate. Further more, it is usually the smallest solution in terms of size and purchase price [13].

In PV application measuring residual currents with shunts is not practical. Residual currents are common-mode so there has to be two measuring points in the circuit, the phase-line and the neural-line. The resistors themselves should be low resistance to minimize the losses. The main currents running through the resistors can be easily in the class of hundreds of amps. Still significantly lower residual currents of 30 mA must be detected. This would cause the resistances to be very low and the voltage measured across them would be minimal and difficult to read. Additionally the two measuring points have to be separated from each other because the voltage difference between the phase and neutral is 230V. It would make the design expensive and complex.

3.2 Current measuring with magnetic sensor

Current flowing through a conductor induces a magnetic field around the conductor. The magnetic field can be measured with a variety of technologies. Usually, a toroidal ring with a high permeability core material is used to capture the magnetic field. The current can be accurately measured through the magnetic field that it induces. The benefit in inductive measuring is the galvanic separation between the primary current wire and the measuring circuit. Galvanic separation is beneficial when the circuits have a high potential difference. Galvanic separation is a safety aspect because the measured circuit in the photovoltaic inverters is connected directly to the

mains voltage. Magnetic measuring is also quite loss less so it is an efficient method to measure high currents.

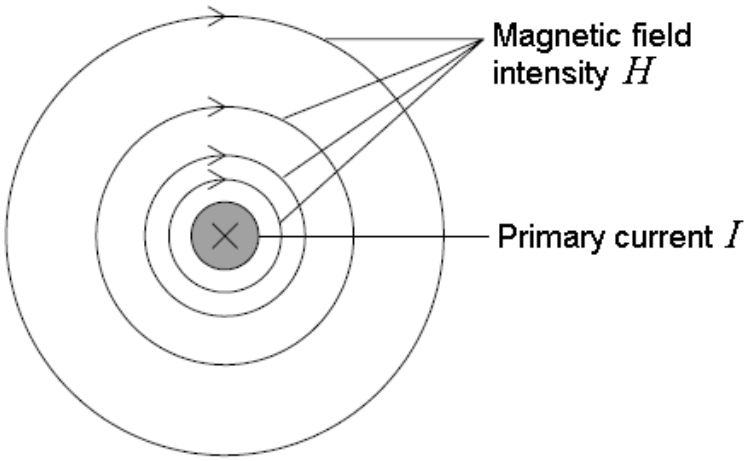

Figure 2: Magnetic field lines around conductor carrying current *I*

The magnetic field strength around the conductor can be calculated using Ampere's law presented in Equation (2):

$$\oint \overline{H} \cdot dl = \overline{I} \qquad \textbf{(2)}$$

Here *H* is the magnetic field strength, *l* is closed path along which *H* is being integrated and *I* is the current in the conductor. The direction of the field lines is defined by the right hand law. The right hand thumb shows the direction of the current while the other fingers show the direction of the magnetic flux density. The relation between magnetic field *B* and magnetic field strength *H* is:

$$\overline{B} = \mu \overline{H} = \mu_0 \mu_r \overline{H} \text{ ,} \qquad \textbf{(3)}$$

where μ is absolute permeability of the material, μ_r is the relative permeability of the material and μ_0 is the absolute permeability of the vacuum.

In this example, the conductor is round and thus the magnetic field strength is constant at a constant distance from the conductor. Equations (2) and (3) can be used for Equation (4):

$$\oint \frac{\overline{B}}{\mu_r \mu_0} dl = \overline{I} \Leftrightarrow \oint \overline{B} dl = \mu_r \mu_0 \overline{I} \quad \textbf{(4)}$$

In this example only air surrounds the conductor, so $\mu_r = 1$. Because the magnetic field strength vector *H* and the magnetic flux density vector *B* are parallel to the closed path unit vector, *dl*, the dot product in Equation (4) can be replaced with normal multiplication. The magnetic field is constant at the chosen loop. The term *B* can be taken outside from the integral.

$$B \oint dl = \mu_0 I \quad \textbf{(5)}$$

The line integral of a round with radius of *r* is $2\pi r$ which is the periphery of a circle. The Equation (5) can be modified to Equation (6) which represents the magnetic flux density at a distance *r* from an infinite long, round conductor that is in free space.

$$B = \frac{\mu_0 I}{2\pi r} \quad \textbf{(6)}$$

Equation (6) shows clearly that the magnetic field is proportional to the current *I* in the conductor and is inversely proportional to the distance r from the conductor.

The relation between *B* and *H* is not linear with all materials. The saturation of the core material causes unlinearity at some point of the B-H-curve. As the current in the conductor increases, the magnetic field strength and the magnetic flux density increase accordingly. At some point the magnetic flux density *B* does not increase at the same rate as the magnetic field strength *H*. As *H* increases even more, the magnetic field *B* starts to asymptotically approach the maximum value B_{sat} of the magnetic flux density. Air core

inductors will not saturate. Air gaps added into a ferromagnetic material will increase the saturation level and the core is less easily saturated.

Ferromagnetic materials are constructed of atomic dipoles. The dipoles align themselves with the external field. The material is saturated when almost all of the dipoles are aligned in the same direction. The B-H-curve also includes hysteresis. Some of the dipoles remain aligned and induce a remanent magnetic field when the external field is removed. The material is now magnetized. The remanent magnetization is B_r in Figure 3. The coercivity of the magnetization is H_c and it means that the magnetic field intensity value at which the magnetic flux density is zero [33].

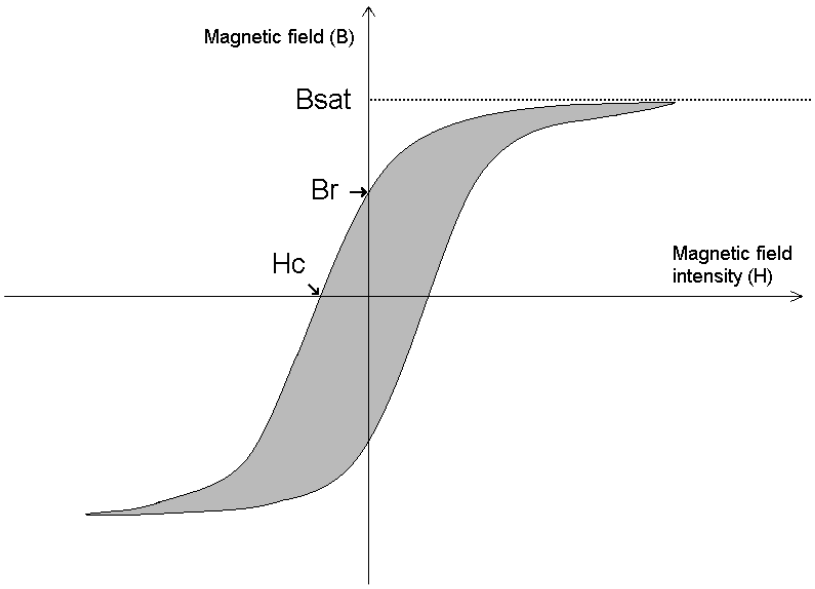

Figure 3: B-H-curve of some material

The losses of the core material per volume are expressed by the gray area of Figure 3, the area presenting the energy lost into the hysteresis [34]. The B-H-curves are a material specific feature. Typical curve types are R-, F- and Z-type of curves. The R-type is a) in Figure 4. It is a round loop and it has high remanent magnetization. The Rectangular loop b) in Figure 4 is called a Z-type. It has high coercivity of magnetization and remanent magnetization.

Also, the losses are high due to the large area inside the loop. The flat loop c) in Figure 4 is called as F-type B-H-curve. It has usually low coercivity of magnetization and remanent magnetization. It also has low losses.

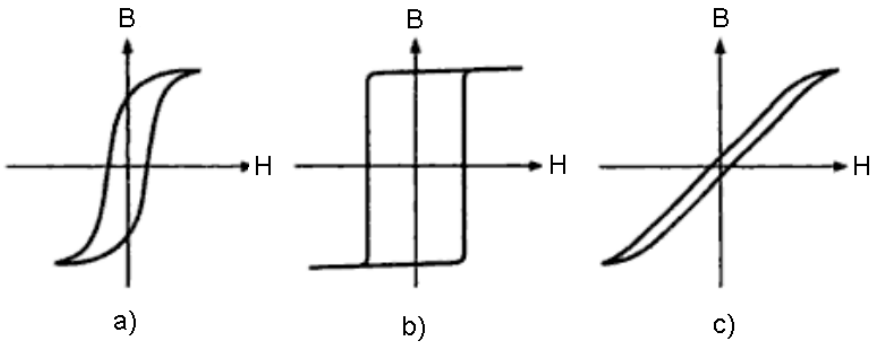

Figure 4: Typical BH-curve types [35]

3.3 Open loop and closed loop systems

Measuring systems in general can be either open loop or closed loop systems. Open loop systems are the ones that do not have feedback from the measurement. On one hand they are usually cheap and not very accurate, making them easily susceptible to errors caused by component tolerance and noise from the measuring environment. On the other hand, they consume less energy than closed loop devices which is beneficial in battery powered applications [3].

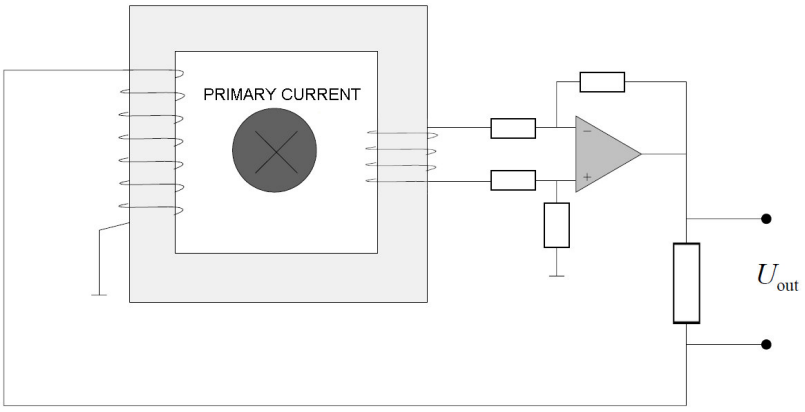

Figure 5: Closed loop system

Closed loop systems have a feedback in the measuring circuit. The feedback usually works as in Figure 5. In magnetic measurements the conductor carrying the primary current pierces a high permeability core. The current in the conductor induces a flux into the core that is measured with some chosen mean. The feedback circuitry controls a feedback winding of the core that tries to eliminate the flux in the core and set it back to zero by inducing a opposite direction flux to the core (Left side winding in Figure 5).

The feedback allows the extension of measuring parameters, for example, allowing the measuring range to be extended. The core is not saturating as soon as in open loop systems because the feedback tries to keep it at zero by applying a reverse polarity flux to the core. The noise levels are also lowered. The output is more linear and the high loop gain makes the output less sensitive to component variation and temperature change. The bandwidth is usually higher in closed loop systems and overall they are more accurate than open loop systems. [3]

3.4 Hall sensor

Hall sensors consist of a hall element and the circuitry driving it, both of which are usually integrated in the same chip. Hall sensors are by far the most used sensor type having a 90 % market share [18]. The Hall Effect utilizes the Lorentz force presented in Equation (7):

$$F = qE + q[v \times B], \quad \textbf{(7)}$$

where q is the particle charge, E is the electric field producing the bias current, v is the charge carrier velocity and B is the normal component of the magnetic field perpendicular to the Hall element.

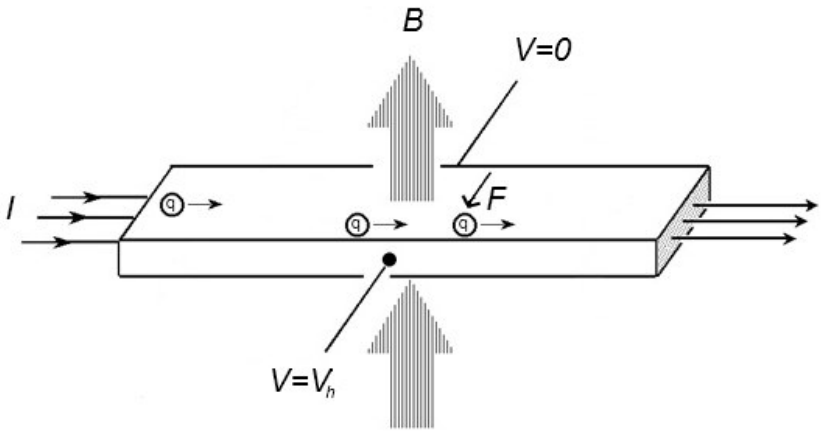

Figure 6: Hall effect

In practice, a voltage is applied across the Hall element. The voltage creates a bias current that flows through the element. The charge carriers of the bias current start to gather on the other side of the hall element due to the Lorentz force *F* when the element is placed in an external magnetic field. This is shown in Figure 6. The concentration of charge carriers on the other side and lack of charge carriers on the opposite side creates a Hall voltage V_h across the Hall element. The Hall voltage increases as long as its force equals to the Lorentz force created. The voltage difference is linearly proportional to the external magnetic field piercing the element [15]. Usage of the hall sensor in current measurement is shown in Figure 7. The magnetic field induced by the primary current is captured by the high permeability toroid. Hall sensor is placed in the air gap of the toroid.

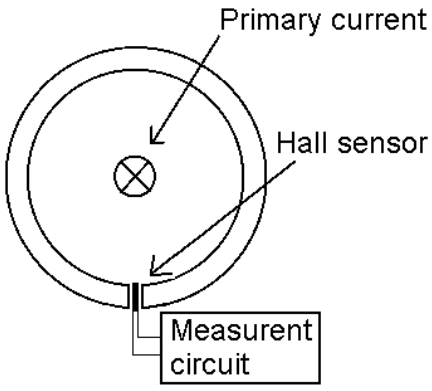

Figure 7: Hall sensor measuring circuit

The Hall elements suffer from low sensitivity to magnetic fields and they have quite a high offset voltage. The sensitivity is in the class of 1 mV/mT for silicon based sensors but more expensive Indium antimonide sensors can achieve 5 times higher sensitivity [18]. The Benefits of Hall sensors are low cost production and their very small package size [14].

3.5 Fluxgate sensor

Fluxgate sensors are widely in use today, being frequently used for current measuring although their main field is in compass navigation. The history of the fluxgate dates back to 1928 and it has been used in submarine detection and airborne magnetic field mapping [15].

Fluxgate is based on two coils wound around one or two high permeability ferromagnetic cores. The first coil is an excitation coil and the second is a pickup coil. Current pulses at frequency f_0 are driven into the excitation coil. The current has to be high enough to saturate the core of the excitation coil. The excitation coil is driven in periods from negative saturation to positive saturation. The core has high relative permeability μ_r when it is not saturated (Figure 8, points 2 and 4). High relative permeability leads to low reluctance as can be seen from Equation (8) [27]:

$$R = \frac{l}{\mu_0 \mu_r A} \tag{8}$$

Here l is the length of the magnetic circuit, μ_0 is the permeability of the vacuum, μ_r is the relative permeability of the material and A is the cross-sectional are of the circuit. The external magnetic field sees the core as a low reluctance path to move when the core is not saturated. The permeability of the core decreases significantly when it is saturated (Figure 8, points 1 and 3). Thus the reluctance of the core increases and the external magnetic field

is driven out of the core. The name flux gate comes from the view that the magnetic field is by turns driven into the core and out of the core. [14][15]

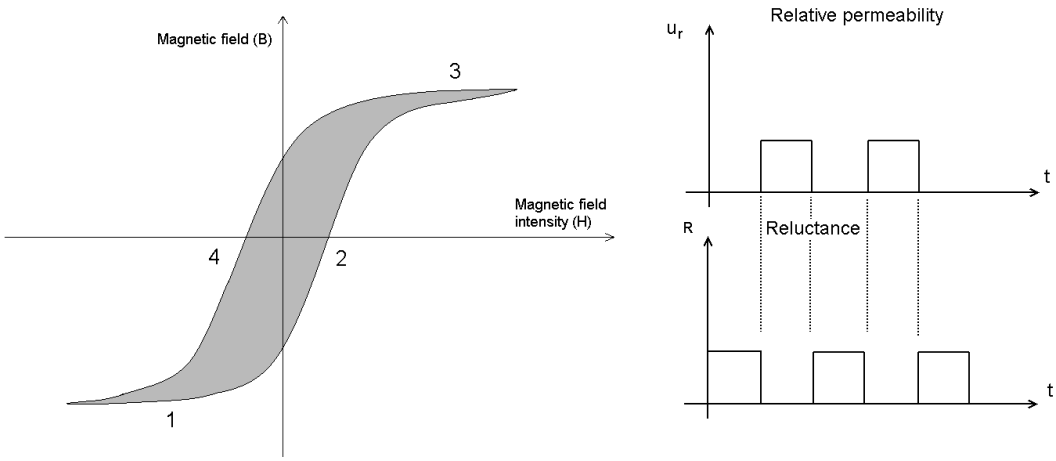

Figure 8: Principle of fluxgate technology

Three primary methods are used to measure the external field B_0 from the voltage induced to the pickup coil:

- Second-harmonic principle
- Pulse-height principle
- Pulse-position principle

The first method examines the amplitude of the second-harmonic $2xf_0$ of the excitation frequency f_0 which is proportional to the external magnetic flux density B_0. The AC signal in the excitation coil at frequency f_0 induces only odd harmonics of f_0 to the pickup coil. Even harmonics are generated to the induced voltage when the pickup coil is subjected to a magnetic field that contains a DC-component. The DC-component is created by the external magnetic flux density B_0.[14]

The second method measures the voltage peaks of the pickup coil. These peaks are caused by the external magnetic field B_0 that increases the voltage peak in one polarity and decreases it in the other polarity. The difference in these negative and positive peaks is linearly related to B_0.[14]

The last method is based on pulse-position. The external magnetic field B_0 causes the sensor to be saturated for a longer time in one direction and for a shorter time in the other direction. This causes the other half period of the induced voltage to be also longer than the other. The change in the pulse width expresses the external magnetic field [16].

The disadvantages of fluxgate sensors are their relatively high cost and large size compared, for example, to the Hall sensors presented in the previous section. The benefits are wide and accurate measuring range [14]. Standard commercial sensor can achieve 10 nT accuracy but better sensors achieve an accuracy of 1nT. The sensitivity of fluxgate sensors is in the range of hundreds of mV/mT [17][18].

3.6 Comparison of methods

Hall sensors have a sensitivity of about 1 mV/mT and fluxgate sensors have a sensitivity of hundreds of mV/mT as presented in the section 3.4. Hall sensors are not sensitive enough to be used in applications measuring low currents. Hall sensors also have higher offset voltages which only decreases the measuring capability of low currents. Fluxgate sensors can be used in low current measurements. They are sensitive enough to measure currents of milliamperes. Comparison between open loop and closed loop operation shows that a closed loop system would be better for measuring low residual currents where reduced noise levels increase the reliability of the measurement.

4 Commercial sensors

No hall sensor based measuring devices were found to measure residual currents. Various current sensor manufacturers were searched for without success. The hall sensors found were designed to measure main currents in various applications, the currents to be measured being in the class of ± 5 A and above.

Suitable fluxgate sensors were easier to find. For the purposes of this thesis the important characteristics to be measured are sensor output in general. This includes the relationship of the output voltage to the primary current and the sensitivity of the sensor to various residual currents. The sensitivity is tested with DC- and AC-current and a combination of these. Temperature behavior is of interest and the characteristics to study are DC-offset and gain drift. Also frequency response is measured.

4.1 Manufacturer A

The offer from manufacturer A is a device that uses ± 15 V supply and draws ± 45 mA current in maximum. The measured RMS current was ± 38 mA. Power consumption is thus $P = 1{,}14$ W. The device has four pins in its connection interface; + V_{CC}, - V_{CC}, GND and V_{OUT}. A 10 kΩ load resistor is externally connected between the V_{out} and GND. Output voltage is ± 5 V. The device can measure residual currents up to ± 400 mA. The frequency range of the device is DC and from 40 Hz to 11 kHz. Frequencies between the DC and 40 Hz are not reliably measured. This can be seen from Figure 9, which shows the output signal of the sensor with a square current pulse of 80 mA at a frequency of 10 Hz.

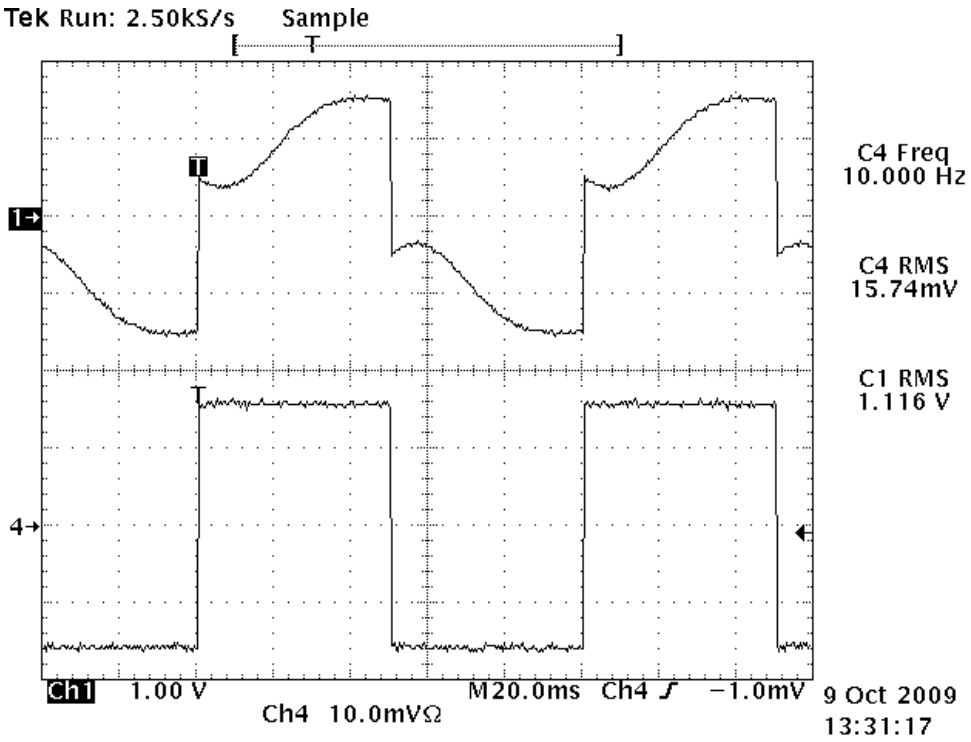

Figure 9: Voltage output of sensor B at frequency of 10 Hz (CH 1 = V_{out} , CH4 = current, 10 mV = 50 mA)

The output signal is clearly distorted in Figure 9 and does not represent the measuring result. The square wave contains a number of sine wave frequencies. The 10 Hz square wave has a sine base frequency of 10 Hz. It also contains the odd harmonics of the base frequency; 30 Hz, 50 Hz, 70 Hz, etc. The low frequency components seem to be missing from the output signal. Figure 10 presents the output signal of the sensor at a frequency of 2 kHz. The output signal is in order and does not need any extra filtering. Tests with sine wave were also performed. The sine wave causes also higher than expected output signal at the frequency range DC to 40 Hz but the output waveform is not distorted.

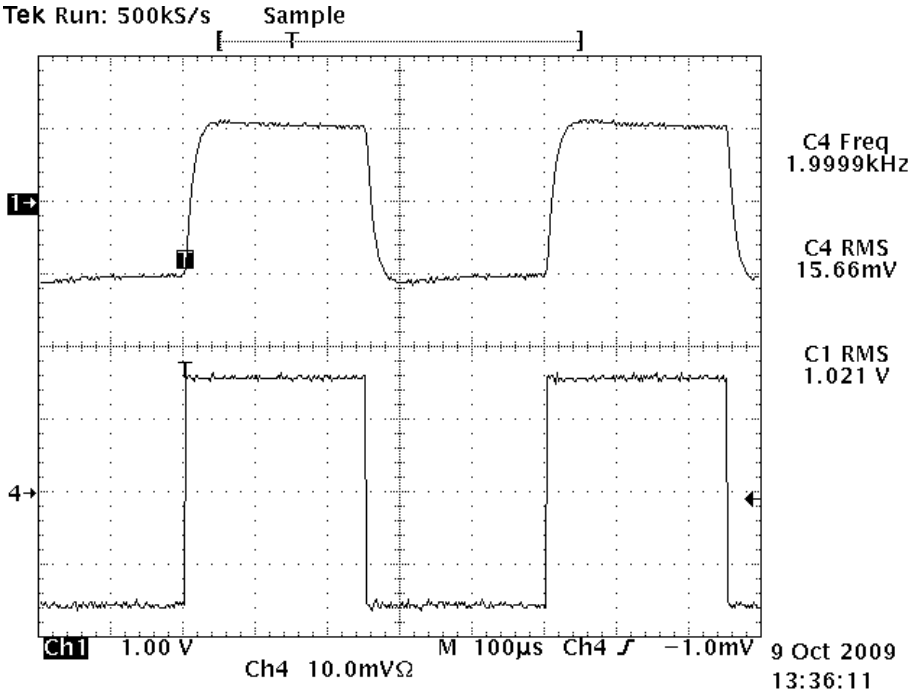

Figure 10: Voltage output of sensor B at frequency of 2 kHz (CH 1 = V_{out} , CH4 = current, 10 mV = 50 mA)

The frequency response and gain drift of the sensor under various temperature conditions is shown in Figure 11. The tests were made with square current waveform and 80 mA current. The output of the sensor is seen to be very stable between the various temperatures. The maximum difference is about 10 mV which is about 1 % of the output signal. The difference in outputs between the frequencies 40 Hz (V_{out} = 940 mV) and 2 kHz (V_{out} = 1040 mV) is 100 mV. It is 10 % of the result and is quite high. The compensation of the unlinearity of the frequency response would require an external amplifier with an accurately specified decreasing frequency response. This would be difficult to implement in practice.

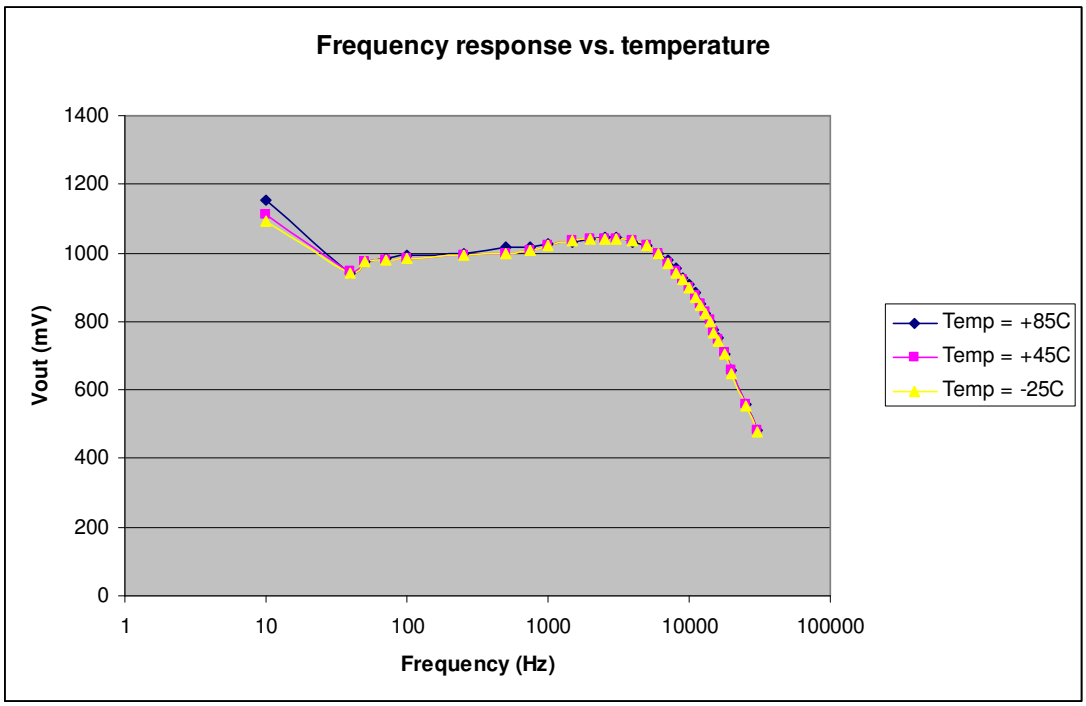

Figure 11: Frequency response and gain drift under various temperature conditions

4.2 Manufacturer B

Manufacturer B offered a device that works with + 5 V supply. It draws 16 mA current at maximum which converts to $P = 5V \times 16\ mA = 80\ mW$ in power consumption. The device also has four pins in the connection interface; V_C, V_{REF} IN/OUT, V_{OUT} and GND. The output is connected to ground via 100 kΩ load resistor. The output signal voltage is between 0 V … 5 V. 2.5 V is the zero level. The nominal residual current to be measured is ± 300 mA but the device can measure currents up to ± 850 mA. The frequency range is from DC to 10 kHz.

Manufacturer B's sensor seemed to create a noise in the + 5 V power supply. Without any filtering capacitors, the ripple was measured to be 70 mV_{p-p}. The frequency of the ripple was ~900 kHz. This was double the frequency of the excitation coil inside. The ripple affected the measuring output and the ripple without filtering was about 50 mV_{p-p}. Supply filtering was done with two 100 nF capacitors parallel in the power supply. The ripple in the + 5 V supply

decreased to 25 mV_{p-p}. The ripple in sensor output signal lowered to 30 mV_{p-p} as in Figure 12.

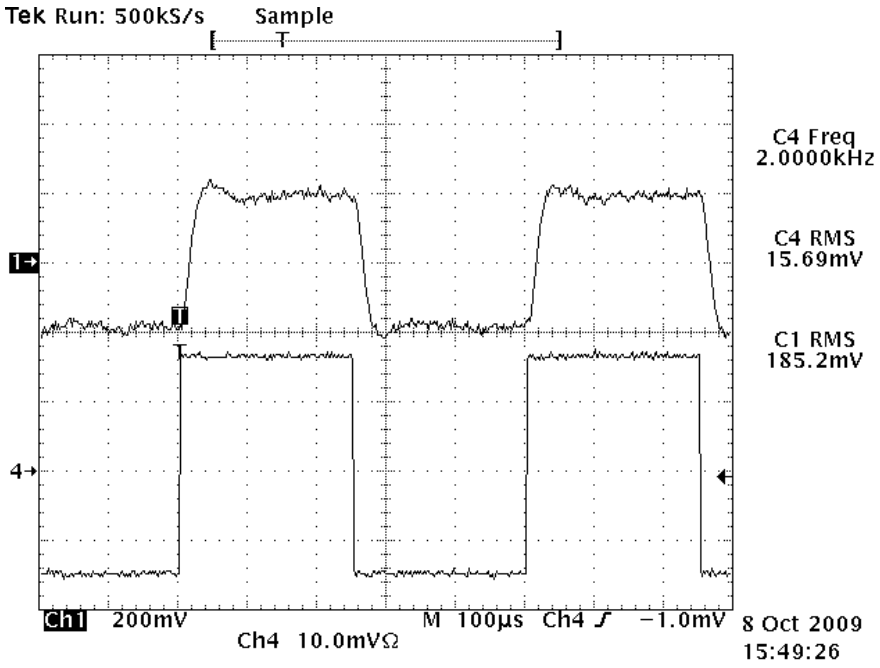

Figure 12: 200 nF supply filtering, 2 kHz 80 mA square current (CH 1 = V_{out} , CH4 = current, 10 mV = 50 mA)

The output signal still contained quite much noise. Therefore, the remaining noise was filtered with an external RC-filter. The value of the resistor was 10 kΩ and the capacitor was 3,3 nF. This created a filter with -3 dB frequency of 4,8 kHz. The ripple in the output signal decreased to less than ten millivolts. The filtered signal can be seen in Figure 13. The sharp corners became round as the high frequency components were filtered. The sine waveform was not altered in the filtering.

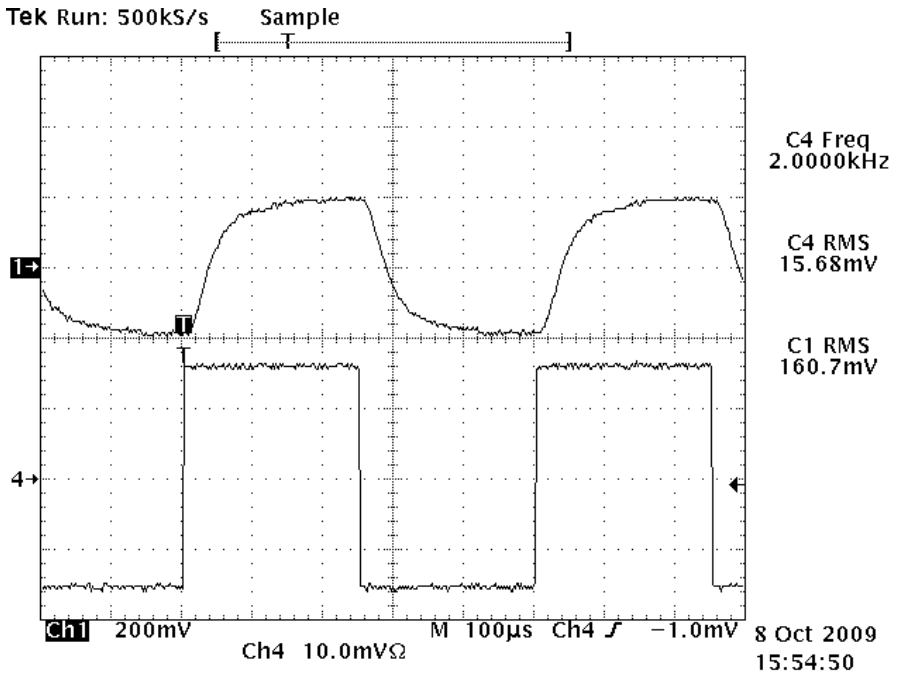

Figure 13: RC-filtered output signal, 2 kHz 80 mA square current (CH 1 = V_{out} , CH4 = current, 10 mV = 50 mA)

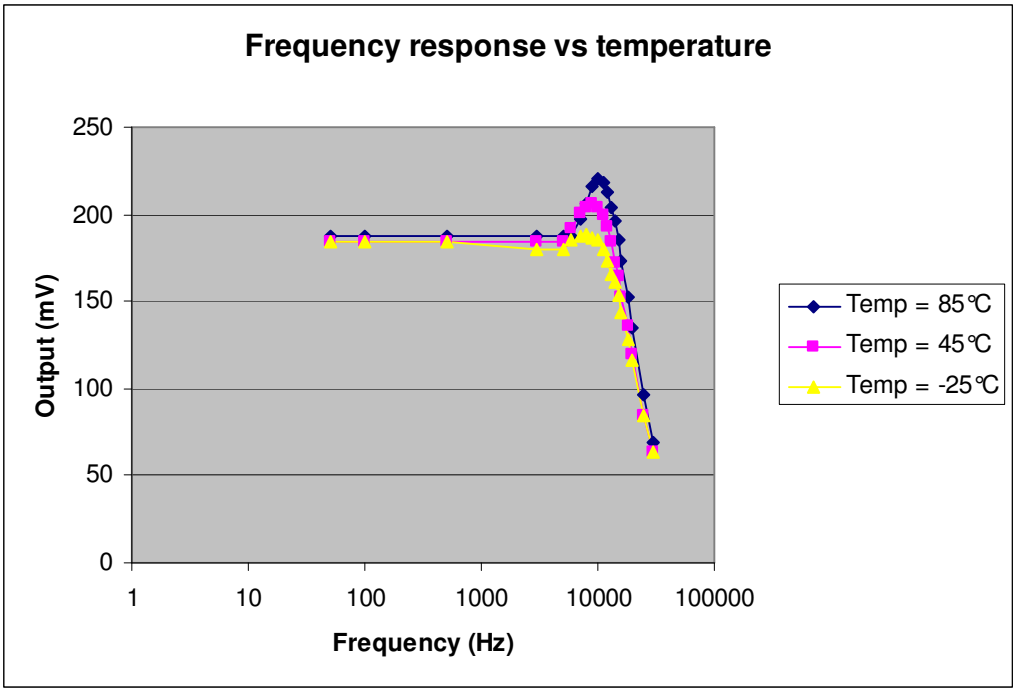

Figure 14: Frequency response and gain drift under various temperature conditions

The frequency response and gain drift of the sensor under various temperatures is shown in Figure 14. The tests were made with a square current waveform and an 80 mA current. The difference between the

measurements is about 4 mV at frequencies lower than 3 kHz. The output of the sensor was 184 mV at a frequency of 100 Hz at room temperature. The temperature error was about 2.2 %. The peak in the frequency response is higher the warmer the ambient temperature is. The response is steady until about 1 kHz. After 1 kHz, it starts to decline slightly. From 5 kHz to about 11 kHz, the frequency response rises. From 11 kHz onwards, the response declines rapidly. The response to the sine waveform is similar to the response to the square waveform.

The V_{ref} voltage was tested against variation in supply voltage and temperature. The reference voltage was 2.499 V when the supply voltage was 5.00 V. A + 10 % change in supply voltage increased the reference voltage by 2 mV. A decrease of – 10 % in supply voltage lowered the reference level by 2 mV. The reference voltage is temperature stable. Tests were made in a temperature range of – 25 °C to + 85 °C. The reference level was steady but near the – 25 °C the voltage dropped by 1 mV. The change, however, is negligible.

4.3 Manufacturer C

The design and structure of the sensor from Manufacturer C was examined. The operation of the sensor could not be verified because the manufacturer did not provide the datasheets containing the specifications. Further testing of the sensor was cancelled because Manufacturer A and Manufacturer B provided well documented solutions.

The technology behind Manufacturer C's sensor is not known. It has an Atmel Mega48 microprocessor as the heart and couple of other ICs. The total component number is 67. The magnetic circuit consists on 3 windings. The yellow and green winding have about the same number of turns. They are wound in the same direction and both coils look like rogowski coils. The red coil is wound around the core in a way similar to a normal toroid coil. The core is manufactured from a hollow plastic toroid which has a metallic strip

wound core inside. The whole package is covered from every side by a metallic shield.

4.4 Comparison of sensors

The sensors produced by manufacturers A and B both fulfill their documented specifications. Differences could be found between the devices and they differed in characteristics. Sensor of Manufacturer A used over 14 times the power of sensor of Manufacturer B. The frequency response of sensor B was stable until 5 kHz. After 5 kHz the frequency response had a peak. The peak in the frequency response was very temperature sensitive and it changed about 10 % between – 25 °C and + 85 °C. Sensor A could not measure frequencies under 40 Hz though it could measure stable DC. The sensor had a high peak in this low frequency range. The response from 40 Hz to 2 kHz increased steadily and was about 10 % higher at 2 kHz than at 40 Hz. Sensor B had a constant response on frequencies under 2 kHz. Sensor A was very stable temperature vice through the whole frequency range. Both sensors performed well in temperature tests in the important frequency range of DC – 2 kHz. Both were very temperature stable excluding the frequency range of DC – 40 Hz from sensor A. Sensor B performed better over all in the important frequency range of DC to 2 kHz.

5 Designing fluxgate prototype sensor

A prototype sensor was built in order to attain more insight into the practical issues of the measurement technology. The prototype sensor should measure residual currents as demanded by the standards. The device built is not a ready commercial product but rather servers as a technology pilot.

The prototype sensor was based on fluxgate technology. The decision was based on the findings in Chapter 3. Two options were found for proceeding with fluxgate technology while studying the literature and the devices available on market. One possibility was to build the whole circuit out of discrete components and operation amplifiers. The other option was to use the IC DRV401 manufactured by Texas Instruments. This IC circuit handles the excitation, compensation and final measuring functions and it has extensive fault detection functionality. The sensor was based on the IC DRV401. It seemed the most efficient solution taking into consideration the time available and the expertise of the developer. The sensor circuit needs about 20 external components besides the IC to operate. These components are resistors, capacitors, diodes and two coils.

A magnetic circuitry is built to sense the magnetic field of the current. Component costs are naturally of concern. For this reason basic toroids, U-cores and similar non-custom made components were tested as the magnetic circuit because they are cost efficient and widely available.

5.1 Specifications

The specification of the device is close to the one of manufacturer B. The device has to be able to measure AC- and DC-currents and combination of these up to ± 300 mA. The maximum frequency of the current measured is 2 kHz by the standard VDE 0126-1-1 and it has to be monitored correctly.

The supply voltage is 5 V and the power consumption target is the same that manufacturer B consumes, 80 mW.

5.2 Designing electric circuit

5.2.1 IC functional description

DRV401 is an IC manufactured by Texas Instruments and it is designed for a wide range of current measuring circuits. It uses the pulse position principle presented in Section 3.5. Depending on the circuit around it, it can measure either low currents, as in this thesis, or high main currents up to hundreds of amperes. It uses a single sided + 5 V supply. It is available in two separate packages; QFN-20 (5 mm x 5 mm) and SO-20 (12,95 mm x 10,65 mm). The pin assignments are shown in Table 2.

Table 2: Pin assignments of DRV401

Pin number	Name	I/O	Description
1	/PWM	Output	PWM output from probe circuit (inverted)
2	PWM	Output	PWM output from probe circuit
3	ERROR	Output	ERROR flag, low active
4	DEMAG	Input	Demagnetizaion enable/disable/start
5	GAIN	Input	Open-loop gain: low = normal, high = -8 dB
6	REF_out	Output	Internal zero reference 2,5 V
7	REF_in	Input	External zero reference
8	V_out	Output	Output for differential amplifier
9	IA_in2	Input	Noninverting input of differential amplifier
10	IA_in1	Input	Inverting input of differential amplifier
11	GND2	Input	Ground
12	I_comp2	Input/Output	Compensation coil driver output 2
13	I_comp1	Input/Output	Compensation coil driver output 1
14	V_dd2	Input	Supply voltage
15	Ccdiag	Input	Wire-break detection, high = enable
16	OVER_RANGE	Output	Over-range indication of V_out, low = over range
17	V_dd1	Input	Supply voltage
18	IS_2	Input/Output	Excitation coil driver output/inout 2
19	GND1	Input	Ground
20	IS_1	Input/Output	Excitation coil driver output/inout 1
Thermal pad		Input	Connected to ground

The main components in the external circuitry are the two coils called the excitation coil and the compensation coil. Other circuitry includes signal filtering and overvoltage protection. The block diagram is shown in Figure 15.

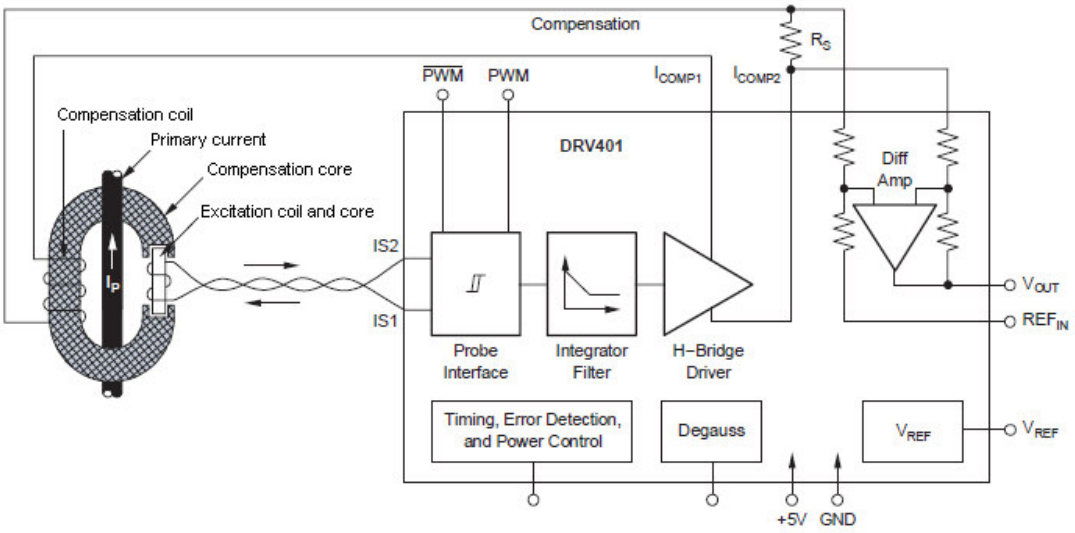

Figure 15: DRV401 Block diagram [19]

The probe interface circuit starts to drive the excitation coil between positive and negative saturation. The voltage over the excitation coil is inverted when the current through it reaches 28 mA. The oscillation frequency of a proper working excitation coil is between 250 kHz and 550 kHz depending on the magnetic properties of the coil. Both half periods of current through the coil are symmetric and equal in duration when no external magnetic field is present. This can be seen in Figure 16. The PWM produced is also symmetric and the integrators output is zero when both half periods are the same in length. No compensation current is created and the output signal of the whole circuit is zero.

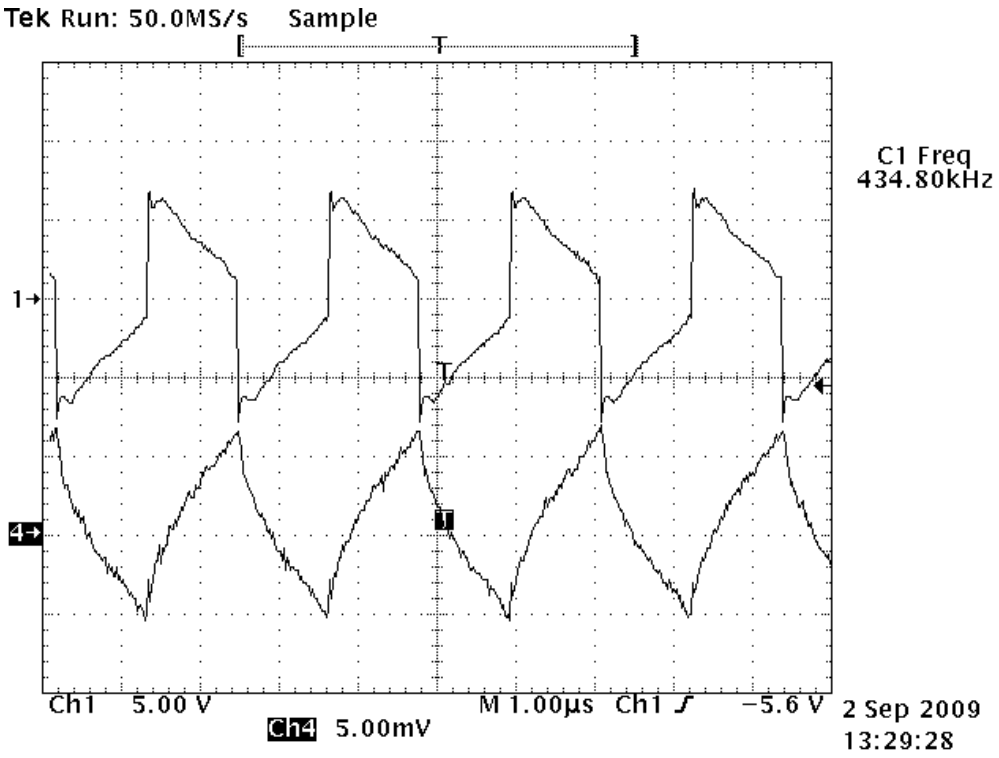

Figure 16: Ch 1 is the voltage over the excitation coil and Ch4 the current through it. No external magnetic field (in Ch4 5.00 mV = 25 mA)

As described in Section 3.5, the pulse position principle reacts to the asymmetry of the saturation times between negative and positive saturation. The saturation half periods start to be asymmetric in duration when an external magnetic field is applied to the excitation coil. The PWM produced is also asymmetric and the internal integrator starts to output a nonzero signal. The nonzero signal drives an H-bridge which further drives the current into the compensation coil. The current in the compensation coil induces a magnetic flux that is in the opposite direction compared to the external flux. The compensation flux tries to cancel the external field influencing the excitation coil. The current flowing through the compensation coil also flows through a shunt resistor (R_S in Figure 15). The voltage over the resistor is measured by a differential amplifier with a gain of four. The voltage output of the differential amplifier is the measurement result. The output can be further filtered if needed.

The DRV401 can measure high frequency currents in a special mode. In this mode the compensation winding acts as the secondary winding of a current transformer and it senses the residual current. The primary current conductor is the single turn primary winding. The H-bridge compensation driver is turned off and in this mode it acts as a low output impedance. The high frequency mode of the IC is not used in this application because the frequencies measured are 2 kHz and below. The range is low frequency and it is measured with the normal mode.

There is a built-in demagnetization system in the IC. The materials of the compensation core are not immune to magnetic remanence, especially the iron cores. Magnetic remanence is produced when a high magnetic field density is applied into the material. Some of the material stays magnetized when the field is removed. The remanence could produce an offset error to the output signal. The built in demagnetization cycle tries to minimize the remanence by driving a series of current pulses to the compensation coil. The demagnetization feature is not used in the prototype.

An extensive fault detection capability is integrated into the IC. The ERROR-pin is pulled low in the case of fault operation. The fault detection acts on low supply voltage (brown-out) and on shorted or open excitation coil. The fault detection discovers also open compensation coil. The open compensation coil is tested when the device is close to maximum modulation. The current through the compensation coil should be greater than 65 mA when close to the maximum modulation. The ERROR-pin is set active (low) if the current is less. This functionality can be disabled by pulling the CCdiag pin low with an external resistor. Open compensation coil detection is not used because the compensation current in normal operation is lower than the required 65 mA. The compensated residual currents are very low, in the class of 30 mA to 300 mA. The use of the open compensation coil detection would cause incorrect fault situations. The OVER-RANGE-pin is set high if the

compensation current in maximum modulation is not enough to compensate the external magnetic field. It will not affect the ERROR-pin.

The DRV401 can drive an external compensation driver to measure and compensate higher primary currents. An external compensation driver might be needed for higher drive voltage and current. The internal voltage gain can lead to instability of the loop when using an external driver. The internal open-loop gain can be suppressed by 8 dB by pulling the GAIN pin high with an external resistor. In this work, only the internal compensation driver is used so the GAIN-pin is connected to ground to keep it low.

Reference input and output pins are included in to the IC. The reference voltage is used as the zero reference to the output signal. The signal output can be adjusted to meet variety of needs by applying an external voltage to the reference input. At the same time the measuring range is reduced as the signal output reaches either rail earlier. The internal reference voltage is 2.5 V and the external reference can be between 0 V and 5 V.

5.2.2 Schematic

The circuit built with the DRV401 is modified from an application note written by Vacuumschmelze [20]. A few connections are included from an example circuit shown in the datasheet of the DRV401 [19]. The entire circuit can be seen in Appendix 1. The bill of materials is included in Appendix 2. All resistors and capacitors were decided to be in a 1206-package to help the assembly of the prototype card. The diodes are basic BAV99 double diodes in the SOT-23 package. The DRV401 package is the SO-20.

The capacitors C1, C2 and C7 filter the supply voltage. C7 is close to the main power connector of the board, C1 filters the supply for V_{DD1} and C2 for V_{DD2}. They all are 100 nF ceramic capacitors. R10 and R9 are 10 kΩ jumper

resistors. They are used to select the demagnetization mode. In the prototype, the DEMAG-pin is pulled low with R9 because the demagnetization feature is not used. R10 is not assembled. The OVER-RANGE is an open-drain output and R8 is a 10 kΩ pull-up resistor for it.

The PWM- and /PWM-pins are high frequency outputs and they are not connected anywhere in the VAC's application note [20]. It was feared that they might cause harm like radiated emissions if unconnected. Thus, 10 kΩ resistors, R13 and R14, were added to ground these outputs. No effects caused by the ungrounded outputs were detected and finally the R13 and R14 were not assembled.

The DRV401 datasheet shows an example circuit for primary current measuring. The circuit has an RC network connected to the /PWM-pin to reduce possible remaining ripple from the excitation coil oscillation. C9, R11, C8 and R12 form the RC-network in the prototype sensor. The RC-network is not used because the output signal is good enough and the possible ripple can be filtered in the signal output filter. R3 and C4 create an RC-filter for the reference voltage input. No external reference is used so REF_{out} supplies the REF_{in}. R2 and C3 create a RC-filter to filter the output signal. R2 is 2.4 kΩ and C3 is 1 nF. The -3 dB frequency is 66.3 kHz. This filters the excitation coil frequency 450 kHz. The -3 dB frequency could be lower to filter the signal even more. The jumper resistor R1 is a 0 Ω resistor to allow the ERROR pin to pull the output down in case of error.

R4, C5, R5 and R6, C6, R7 form two equal RC low-pass T-filters. Both filter the excitation coil oscillation ripple from the compensation coil signal. R6, R7 R4 and R5 are 620 Ω ± 0.5 % precision resistors. Both C5 and C6 are 10 nF and, together with the resistors, they create a filter which has a -3 dB frequency of 25,7 kHz. This filters effectively the 450 kHz excitation coil oscillation ripple. Precision resistors are used for R4, R5, R6 and R7 because

R4 is the shunt resistor which the differential amplifier uses to measures the voltage.

The diodes D1, D2, D3 and D4 protect the T-filters. Rapid changes in the primary current can induce significant current pulses in the compensation coil. Without the diodes these pulses might destroy the T-filter components. The pins I_{comp1} and I_{comp2} can handle high current pulses. IA_{IN1} and IA_{IN2} need external protection to limit the voltage under 10 V of the supply voltage. A double diode D5 is used for the protection. It shorts all high voltage pulses to ground or 5 V supply and protects the inputs IA_{IN1} and IA_{IN2}. The pins IS_1 and IS_2 can handle ± 75 mA currents and are not externally protected in the prototype.

The layout of the prototype board is shown in Appendix 3.

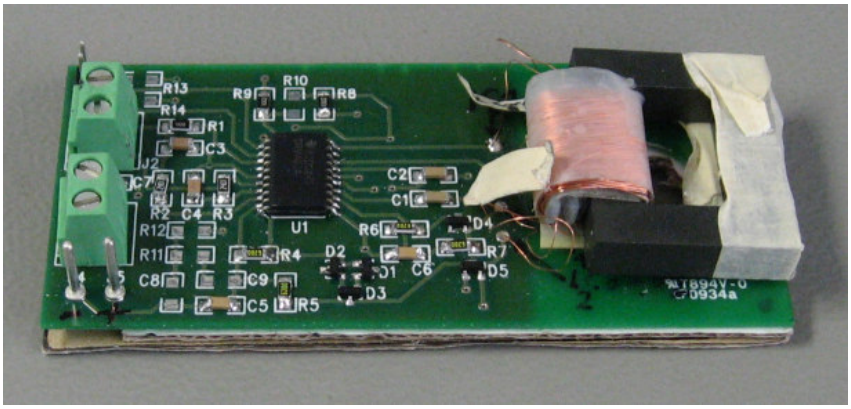

Figure 17: Fluxgate prototype sensor

5.3 Flux gate sensor analytical study

The magnetic circuit can be built in various styles. First, the individual possibilities are identified and calculated. Then they are simulated with Ansoft's Maxwell V.12 magnetic simulating software to obtain a more accurate result.

The equal parts of incoming and outgoing main currents cancel the magnetic field of each other. The residual part induces a magnetic field around the conductors. For simplicity, only one conductor carries the residual part of the main current in the following calculations. In reality there will be two conductors piercing the magnetic circuit. The fluxgate sensor is essentially a current transformer. The residual current part is referred to further on in the text as the primary current, as the term fits better when describing the operation of a current transformer.

5.3.1 Excitation coil and core

It is important to know how the winding turns, the core material and the dimension affect the excitation probes operation. The rise time of the current flowing through an inductance is calculated in Equation (9):

$$\frac{di}{dt} = \frac{v_{\text{ind}}}{L} \tag{9}$$

Here *di/dt* is the derivate of the current with respect to time, v_{ind} is the voltage induced and *L* is the inductance [32]. The increasing inductance *L* decreases the current rising time and the oscillation frequency decreases. The inductance of an object is calculated in Equation (10):

$$L = \frac{\mu_0 \mu_{\text{r}} N^2 S}{d} \tag{10}$$

Here μ_0 is the permeability of the vacuum, μ_{r} is the relative permeability of the core material, *N* is the number of turns in the coil, *S* is the cross area of the coil and *d* is the length of the coil [32]. This shows that the higher permeability of the core material increases the inductance. The number of turns increases the inductance by the power of two. Any increase in the cross area of the winding also increases the inductance. An increase in the width of the winding, on the other hand, decreases the inductance.

5.3.2 U compensation core with toroid excitation core

The U-core used for the compensation coil is as in Figure 18. The core is manufactured by Ferroxcube and the core material is 3E27. The Ferroxcube type number is U25/16/6-3E27[24]. An air gap of 1mm width is left between the two U-cores. The inner diameter of the U-core is 12.7 mm and the outer diameter is 25.4 mm. The length of the leg is 9.5 mm. The core is 6.4 mm in height.

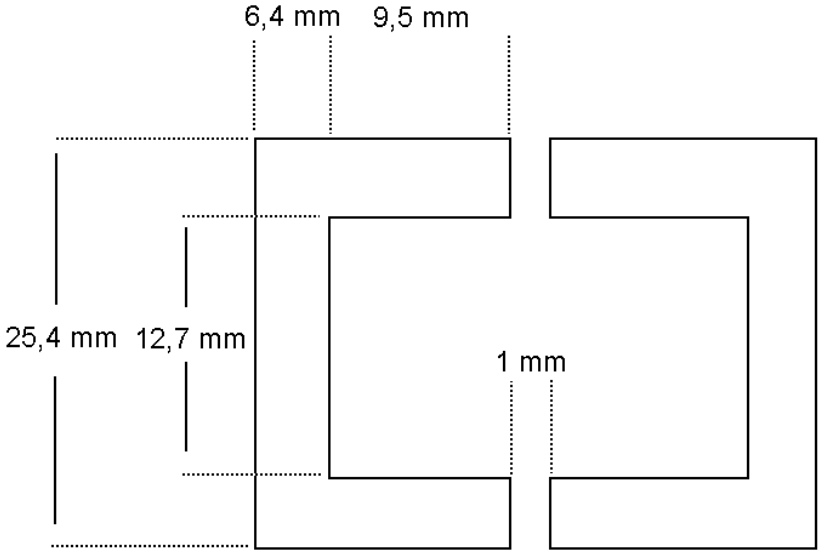

Figure 18:Diameters of the U-cores used

The toroidal excitation core in these calculations is manufactured from Vitrovac 6025Z stripes [28]. The stripes are 20 µm thick and 5 mm wide. The material has a Z-type square B-H-loop and the permeability is in the class of hundreds of thousands or about a million. The core saturates easily because of the square B-H-curve. The magnetic field density in saturation is 0.58 T and it is achieved with very low magnetic field strength. Core losses are also low. The idea is to connect the cores as in Figure 19, in such a way that magnetic induction occurs between the cores. The toroidal excitation core is manufactured from one strip. The cross area is minimized and the magnetization needed for the core to saturate is minimum. The diameter of the toroid is 10.7 mm. The U-core and the toroid are separated by a 1 mm air gap on both sides.

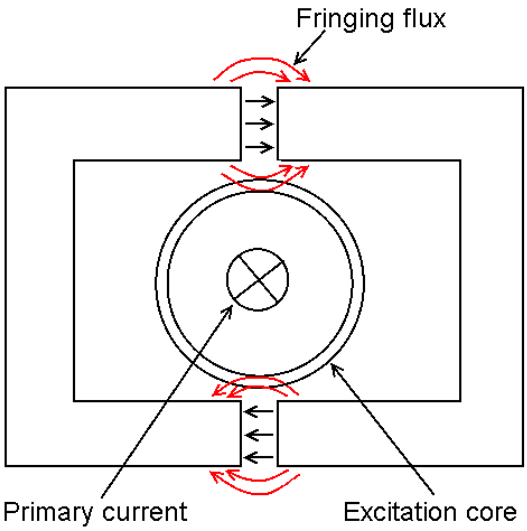

Figure 19: Connection of the two cores

The effective length of the two U-cores without air gaps can be approximated by calculating the perimeter of the core using the average of the external and internal diameter. The effective length without air gaps is used to calculate the effective permeability of the compensation core.

$$l_{e,u-core} = \frac{(25.4\,\text{mm} \cdot 2 + (6.4\,\text{mm} + 9.5\,\text{mm}) \cdot 4) + (12.7\,\text{mm} \cdot 2 + 9.5\,\text{mm} \cdot 4)}{2} = 88.9\,\text{mm} \quad \textbf{(11)}$$

The effective length $l_{e,toroid}$ of the 20 µm strip toroid core is calculated using only the diameter of the core.

$$l_{e,toroid} = \pi \cdot d = \pi \cdot 10.7\,\text{mm} = 33.6\,\text{mm} \quad \textbf{(12)}$$

The effective permeability of the two U-cores with air gaps is as in Equation 12[21]:

$$\mu_e = \frac{\mu_c \cdot \mu_0}{1 + \frac{\mu_c \cdot l_g}{l_e}}, \quad \textbf{(13)}$$

where μ_c is the relative permeability of the core material ($\mu_c = 4130$), μ_0 is the permeability of the vacuum ($\mu_0 = 4\pi \cdot 10^{-7}$ N/A^2), l_g is length of air gaps

(l_g = 2 x 1 mm = 2 mm), and l_e is the effective length of the U-core without gapping ($l_{e,u\text{-}core}$ = 88.9 mm).

$$\mu_{e,u-core} = \frac{4130 \cdot 4\pi \cdot 10^{-7} \frac{N}{A^2}}{1 + \frac{4130 \cdot 2\,mm}{88.9\,mm}} = 4\pi \cdot 10^{-7} \frac{N}{A^2} \cdot 44 = 54 \cdot 10^6 \frac{N}{A^2} \quad \textbf{(14)}$$

The primary current induces magnetic field strength H_{ex_pri} to the excitation core as in Equation (15).

$$H_{ex\_pri} = \frac{I_{pri}}{l_{e,\,toroid}} = \frac{30\,mA}{33.6\,mm} = 0.89 \frac{A}{m} \quad \textbf{(15)}$$

I_{pri} is the primary current. H_{ex_pri} is the magnetic field intensity that has to be compensated to zero. The primary current induces magnetic field strength H_{comp_pri} to the compensation core as in Equation (16).

$$H_{comp\_pri} = \frac{I_{pri}}{l_{e,\,u-core}} = \frac{30\,mA}{90{,}9\,mm} = 0{,}33 \frac{A}{m} \quad \textbf{(16)}$$

Here the $l_{e,\,u\text{-}core}$ is the effective length of the two U-cores with the two 1 mm air gaps. This field strength causes magnetic flux density as in Equation (17):

$$B_{u-core\_ir} = \mu_{e,u-core} \cdot H_{comp\_ir} = 4\pi \cdot 10^{-7} \frac{N}{A^2} \cdot 44 \cdot 0.33 \frac{A}{m} = 18.2\mu T \quad \textbf{(17)}$$

This induces a magnetic field strength of (18) in to the air gaps:

$$H_{gap\_ir} = \frac{B_{u-core\_ir}}{\mu_0} = \frac{18.2\,\mu T}{4\pi \cdot 10^{-7} \frac{N}{A^2}} = 14.48 \frac{A}{m} \quad \textbf{(18)}$$

The magnetic flux has a tendency to fringe out from an air gap that is placed in the magnetic path. Flux fringing depends on the dimensions and the geometry of the whole magnetic circuit. The wider the air gap is the more the flux fringes. The effective cross area of the core increases as the flux fringes. This increase can be approximated with equations but not very precisely.

Two equations were found to offer an approximation. The effective radius r_{eff} is shown in Equation (19)[22]:

$$r_{\text{eff}} = r + \left(0.241 + \frac{1}{\pi}\ln\left(\frac{b_{\text{a}}}{l_{\text{g}}}\right)\right)\cdot l_{\text{g}} = 3.2\,\text{mm} + \left(0.241 + \frac{1}{\pi}\ln\left(\frac{9.5\text{mm}}{1\text{mm}}\right)\right)\cdot 1\text{mm} \quad \textbf{(19)}$$
$$= 3.2\,\text{mm} + 0.96\,\text{mm} = 4.16\,\text{mm}$$

Here r = 3.2 mm is the physical radius of the core, b_{a} = 9.5 mm is the total inside length of the limb containing the air gap and l_{g} = 1 mm is the length of the air gap. A rougher approximation is that the flux fringes out the amount of the air gap length itself [23]. Thus the effective radius would be r_{eff} = 3.2 mm + 1 mm = 4.2 mm. The first approximation is taken into use as it is stricter.

The area of the actual core is 6.4 mm x 6.4 mm = 41 mm^2 and the area of the effective core is 8.32 mm x 8.32 mm = 69 mm^2. The effective area is 68 % larger than the actual core area. Thus 68 % of the flux flows through the fringing flux. The excitation core height is 5 mm. The total perimeter of the effective area is 4 x 8.32 mm = 33.28 mm. The excitation core can sense 5 mm / 33.28 mm * 100 % = 15 % of the fringing flux around the U-cores one air gap. One air gap delivers 0.68 x 0.15 x 100 % = 10 % of the total flux inside the U-core to the excitation core. The excitation core can sense all together 20 % of the total flux inside the U-core because the excitation core senses both air gaps. The sensing factor k is introduced to symbolize the percent of the flux that can be sensed with the excitation core. Here k = 0.2.

This is a very rough estimation. It is used as an estimation because no better means of calculation were found. In reality the fringing flux decreases rapidly as a function of the distance from the core edge. On the other hand the excitation core is manufactured from a material with high permeability. The high permeability offers a low reluctance path for the fringing flux. Thus a higher value of fringing flux flows near the excitation coil. Unfortunately, no analytical means exist to calculate the fringing flux.

The compensation coil induces a magnetic field into the U-core. It can be calculated with Equation (20):

$$H_{\text{comp\_coil}} = \frac{N \cdot I}{l_{\text{e, u-core}}} \quad \textbf{(20)}$$

N is the number of turns over the compensation core, and *I* is the current in the compensation coil. The value of the current is derived from the circuit in an application note [20]. The circuit has 4 x 620 Ω resistors on the compensation coil current path. The output of the IC can drive 5 V to this current circuit. The current in the path is $I = 5\ \text{V} / 2480\ \Omega = 2\ \text{mA}$ at maximum. The winding resistance is estimated to be very low compared to the other resistances and is not added to the calculation.

First, the compensation current has to overcome the magnetic field strength induced to the compensation core. Second, it has to induce a magnetic field from which $k * 100\ \% = 20\ \%$ is used to compensate the field strength in the excitation core. The field strength $H_{\text{comp\_coil}}$ needed to compensate the fields of the primary current is calculated using the magnetic flux density shown in Equation (21).

$$B_{\text{u-core\_pri}} = \mu_{\text{e,u-core}} \cdot \left(H_{\text{comp\_coil}} - H_{\text{comp\_pri}}\right) \quad \textbf{(21)}$$

Here the compensation coil induces the magnetic field strength $H_{\text{comp\_coil}}$ and the field strength $H_{\text{comp\_pri}}$ induced by the primary current is subtracted. This flux density in the air gap turns into magnetic field strength of (22):

$$H_{\text{gap\_comp}} = \frac{B_{\text{u-core\_pri}}}{\mu_0} \quad \textbf{(22)}$$

The amount of sensing factor $k = 0.2$ (20 %) is used from the field strength in the air gap to compensate the field strength in the excitation core. In Equation (23) the magnetic field strength needed to the compensation core is calculated using Equations (15), (21) and (22).

$$H_{\text{ex\_pri}} = k \cdot H_{\text{gap\_comp}} = k \frac{B_{\text{u-core\_pri}}}{\mu_0} = k \frac{\mu_{\text{e,u-core}}}{\mu_0} \left(H_{\text{comp\_coil}} - H_{\text{comp\_pri}} \right)$$

$$H_{\text{comp\_coil}} = \frac{\mu_0}{k \cdot \mu_{\text{e,u-core}}} H_{\text{ex\_pri}} + H_{\text{comp\_pri}} \qquad \textbf{(23)}$$

$$= \frac{4\pi \cdot 10^{-7} \frac{\text{N}}{\text{A}^2}}{0.2 \cdot 4\pi \cdot 10^{-7} \frac{\text{N}}{\text{A}^2} \cdot 44} \cdot 0.89 \frac{\text{A}}{\text{m}} + 0.33 \frac{\text{A}}{\text{m}} = 0.39 \frac{\text{A}}{\text{m}}$$

The number of turns of the compensation coil to compensate the 30 mA primary current can be calculated with Equation (24) that is modified from Equation (20).

$$N = \frac{H_{\text{comp\_coil}} \cdot l_{\text{e,u-core}}}{I} = \frac{0.39 \frac{\text{A}}{\text{m}} \cdot (88.9\text{mm} + 2\text{mm})}{2\text{mA}} = 18 \; turns \qquad \textbf{(24)}$$

180 turns are needed to compensate the primary current of 300 mA.

5.3.3 U compensation core with strip excitation core

The idea is to connect the cores as in Figure 20. The U-cores used for the compensation core are the same as used in Section 5.3.2. One or two excitation cores can be used. In this example, only one excitation core is used for simplicity. The excitation core is 20 µm thick, 5 mm high and 10 mm long.

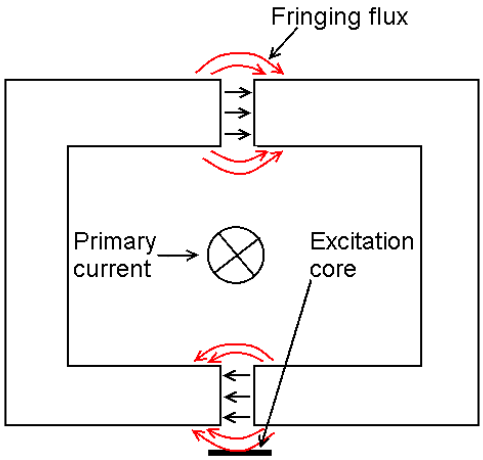

Figure 20: U compensation core and strip excitation core

The major change compared to the calculations in Section 5.3.2 is the magnetic field strength induced in the excitation core from the primary current. The excitation core is now outside the compensation core. The primary current induces magnetic field strength H_{ex_pri} to the excitation core as in Equation (25):

$$H_{ex\_ir} = \frac{I_{pri}}{2\pi \cdot r} = \frac{30\,\text{mA}}{2\pi \cdot 13.75\,\text{mm}} = 0.35\,\frac{\text{A}}{\text{m}} \quad \textbf{(25)}$$

I_{pri} = 30 mA is the primary current, r = 13.75 mm is the distance from the current conductor to the excitation core. H_{ex_ir} is the flux density that has to be compensated to zero. The 30 mA primary current induces a magnetic field strength of H_{comp_pri} = 0.33 A/m to the compensation core as calculated in Equation (16). The corresponding magnetic flux density is $B_{u\text{-}core\_pri}$ = 18.2 µT. The field strength in the air gaps is H_{gap_pri} = 14.48 A/m. The strip excitation core near the air gap is the same size as the toroid excitation core as in Section 5.3.2. The single excitation core can also sense 10 % of the total flux in the U-core. The sensing factor k is now k = 0.1. The magnetic field strength needed for the compensation core can be evaluated using Equation (22). The result is H_{comp_coil} = 0.41 A/m. The compensation coil turns needed to induce this magnetic field strength are calculated with Equation (24). The result is 19 turns. Therefore, 190 turns are needed to compensate 300 mA primary current.

5.3.4 Toroidal compensation core with strip excitation core

The dimensions of the toroid are chosen so that the effective magnetic path length is the same as in the U-core with the air gaps used in the previous chapter, $l_{e,toroid}$ = 90.9 mm . The cross section of the toroid is square and its width and height are 6.4 mm like the U-cores used earlier. The inner diameter of the toroid is 22.53 mm and the outer diameter is 35.33 mm.

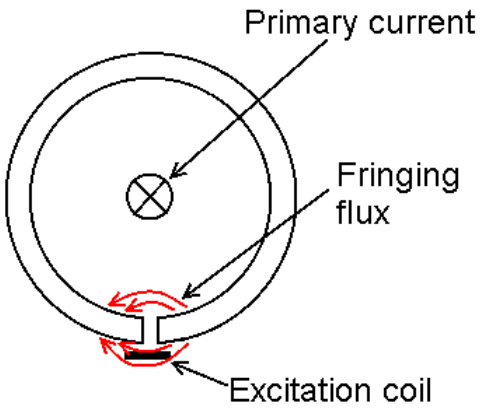

Figure 21: Toroid based solution

The idea of using the toroid is shown in Figure 21. The air gap affects the permeability of the toroid and it can be calculated with the equation (13) and the result is as in Equation (26). The relative permeability is 4130, the effective magnetic length of the toroid is $l_{e,toroid}$ = 90.9 mm and the length of the air gap is 1 mm.

$$\mu_{e,toroid} = \frac{4130 \cdot 4\pi \cdot 10^{-7} \frac{N}{A^2}}{1 + \frac{4130 \cdot 1\,mm}{90.9\,mm}} = 4\pi \cdot 10^{-7} \frac{N}{A^2} \cdot 89 = 112 \cdot 10^{6} \frac{N}{A^2} \qquad \textbf{(26)}$$

The magnetic field strength H is induced into the toroidal compensation core by the primary current as in Equation (27).

$$H_{comp\_pri} = \frac{I_{pri}}{l_{e,toroid}} = \frac{30\,mA}{90.9\,mm} = 0.33 \frac{A}{m} \qquad \textbf{(27)}$$

Here I_{pri} = 30 mA is the primary current and $l_{e,toroid}$ = 90.9 mm is the effective length of the toroid. The field strength at the point of the excitation core, 1 mm outside of the toroid is as in (28).

$$H_{ex\_pri} = \frac{I_{pri}}{l} = \frac{30\text{mA}}{\pi \cdot (35.33\,\text{mm} + 1\,\text{mm})} = 0.26\frac{\text{A}}{\text{m}} \quad \textbf{(28)}$$

Here *l* is the perimeter of a circle that has a radius equal to the distance between the excitation coil and the wire carrying the primary current. The magnetic flux density *B* in the toroid is:

$$B_{toroid} = \mu_{toroid} \cdot H_{comp\_pri} = 4\pi \cdot 10^{-7}\,\frac{\text{N}}{\text{A}^2} \cdot 89 \cdot 0.33\frac{\text{A}}{\text{m}} = 36.9\mu\text{T} \quad \textbf{(29)}$$

The magnetic field strength in the air gap is

$$H_{gap\_ir} = \frac{B_{toroid}}{\mu_0} = \frac{36.9\mu\text{T}}{4\pi \cdot 10^{-7}\,\frac{\text{N}}{\text{A}^2}} = 29.36\frac{\text{A}}{\text{m}} \quad \textbf{(30)}$$

The rule of thumb presented in [23] is used to approximate the effective area used by the magnetic field strength. Also, in this case the air gap is 1 mm and the flux fringes 1mm out of the core. Equation (19) is meant for U- and E-cores and is not used in the case of a toroidal core. The cross-sectional area of the physical gap is 6.4 mm x 6.4 mm = 40.96 mm^2, making the effective area is 8.4 mm x 8.4 mm = 70.56 mm^2. The area increases by 72 %. Thus 72 % of the flux flows through the fringing flux.

The excitation coil height is 5mm. The total perimeter of the effective area is 4 x 8.4 mm = 33.6 mm. The excitation of the coil can sense about 5 mm / 33.6 mm * 100 % = 14.9 % of the flux around the air gap of the toroid. The excitation coil can sense 0.149 x 0.72 x 100 % = 11% of the total flux inside the toroid, k = 0.11.

The field strength needed to compensate the primary current is calculated using Equation (23). Here H_{gap_comp} is the magnetic field strength in the air gap induced by the compensation coil, B_{toroid} is the magnetic flux density

inside the toroid, H_{comp_coil} is the field strength in the toroid induced by the compensation coil and H_{comp_pri} is the field strength in the toroid induced by the primary current. The result is H_{comp_coil} = 0.36 A/m. The coil turns needed to compensate a 30 mA primary current in the toroidal sensor is calculated with Equation (24). The result is 17 turns. To compensate 300 mA there have to be 170 turns of the compensation coil.

5.3.5 Conclusions from analytical study

The calculations showed that it could be possible to sense and compensate primary currents in the range from 30 mA to 300 mA. All the models showed similar results and it was decided to simulate all three models. The toroidal compensation core induces the highest magnetic field in the air gap. This is due to the lack of the second air gap that is present in the compensation core compiled of two U-cores. The second air gap halves the effective permeability of the core and thus less magnetic flux density is induced into the two U-cores. The two U-cores can also be manufactured so that they create one air gap. The rough approximation of the compensation coil turns can be tested with the simulations.

5.4 Fluxgate sensor numerical simulations

5.4.1 U compensation core with toroid excitation core

A simulation model according to the dimensions used in Section 5.3.2 was made. The conductor carrying the primary current I_{pri} = 30 mA is in the middle of Figure 22. The conductor pierces a narrow excitation core. The current in the conductor flows towards the reader creating counter-clockwise field lines. A return wire for the current is needed for the simulation model. It is placed far above the model so that it will not interfere with the magnetic fields studied. The compensation core compiled of two U-cores is placed around the excitation core. The compensation coil is placed around the left U-core forming half of the compensation core. The coil is seen in the figures as two narrow bars on both sides of the left compensation core. The compensation

coil carries the compensation current $I_{comp.}$ The compensation current is actually the ampere turns of the coil in amperes. The number of turns is not needed in simulation of the magnetic fields and I_{comp} is the current flowing through the N-turns multiplied by the number of turns N. The compensation current flows in such a way that it induces clockwise field lines in the compensation core.

Figure 22 simulates the magnetic field strength when no compensation current exists. The primary current is 30 mA. The simulation shows a magnetic field strength of 14.47 A/m in the air gaps. It is very near the calculated result 14.48 A/m of Equation (18). The flux fringes more than the analytical calculations estimated. The outermost light blue region in the upper air gap fringes 5.8 mm out from the core and it represents a field strength of 0.74 A/m. Magnetic field strength of 4.28 A/m fringes about 1.0 mm out from the core. The magnetic flux fringes more near the high permeability excitation core than elsewhere. The high permeability material offers a low reluctance path for the flux.

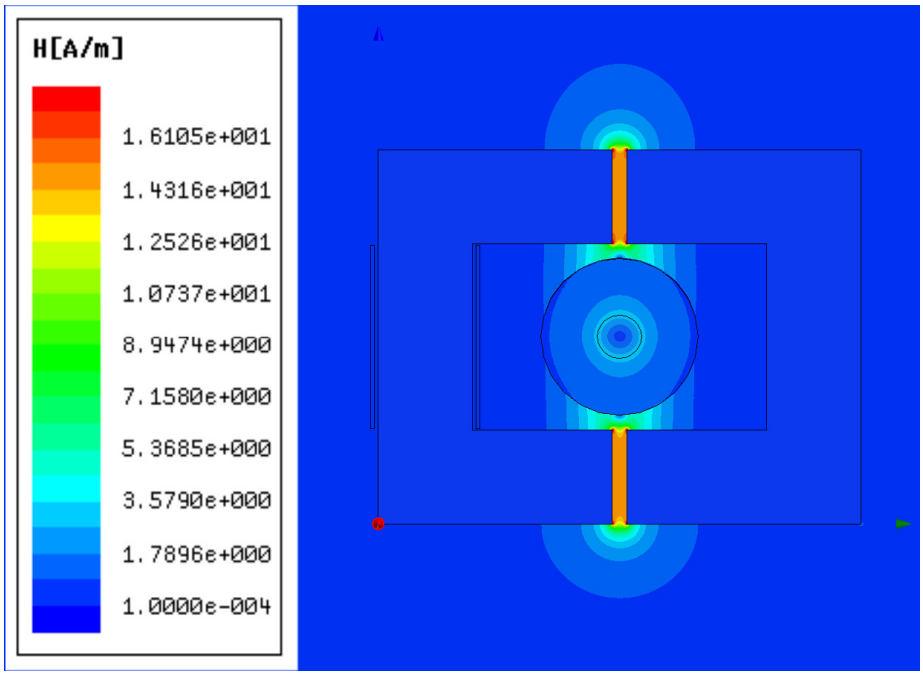

Figure 22: Simulated U-compensation core with toroid excitation core. I_{comp} = 0 mA, I_{pri} = 30 mA

A compensation current of 36 mA is applied in Figure 23. The magnetic field strength in the air gap is 0.32 A/m and is clearly lower than in Figure 22. It is not, however, zero or very near to zero. The I_{comp} needed to cancel the magnetic field induced by the primary current is close to 29 mA when simulated further. Figure 23 shows that the magnetic field strength distributes unevenly around the air gap and the excitation core. It is detected that the toroid is not an efficient shape for the excitation core when studied further. The flux short cuts through the left half of the toroid. This might cause problems in further design. The coil around the excitation core is the sensing element of the circuit. It is difficult to calculate what the excitation coil senses if the magnetic field strength is unevenly distributed inside the coil.

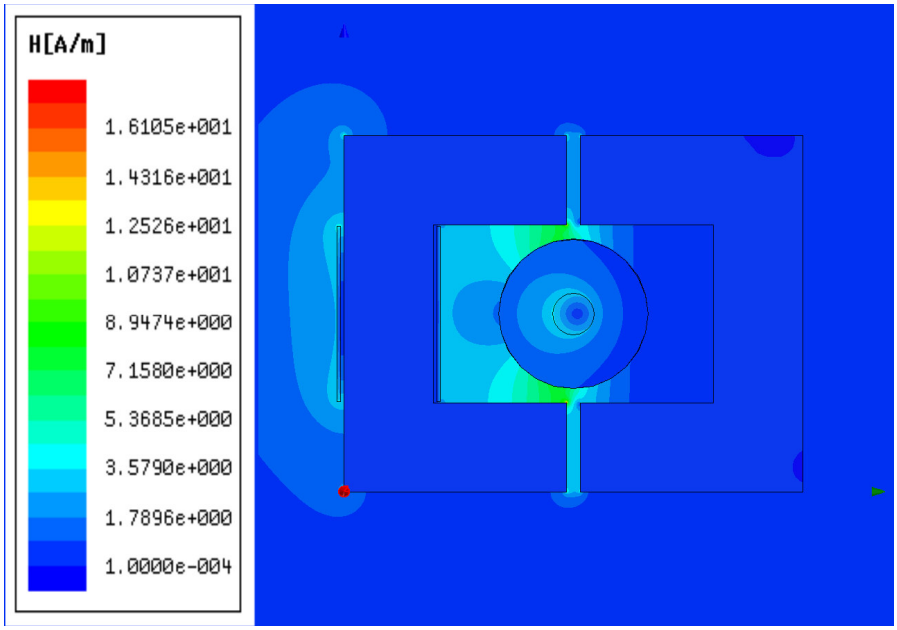

Figure 23: Simulated U-compensation core with toroid excitation core. I_{comp} = 36 mA, I_{pri} = 30 mA

5.4.2 U compensation core with strip excitation core

The model used is as in the previous chapter with the exception of the toroidal excitation core being replaced with a strip excitation core. The excitation core is placed under the lower air gap. The distribution of magnetic field strength can be seen in Figure 24. The field strength is higher in the

upper air gap compared to the lower air gap. The flux uses a wider area in the lower air gap because the high permeability excitation core near the air gap offers a low reluctance path for the flux. This explains the lower magnetic field strength in the lower air gap. The field strength in the upper air gap is 16.40 A/m. The calculated value is 14.48 A/m. The magnetic field strength in the air gaps of Figure 22 is 14.47 A/m. The difference is caused by the toroidal excitation core in Figure 22. The flux uses the toroidal core as a short cut and the whole magnetic flux of the compensation core does not flow through the air gap. The field strength near the current conductor differs from the earlier chapter. The magnetic flux does not short cut anymore from the middle of the compensation core.

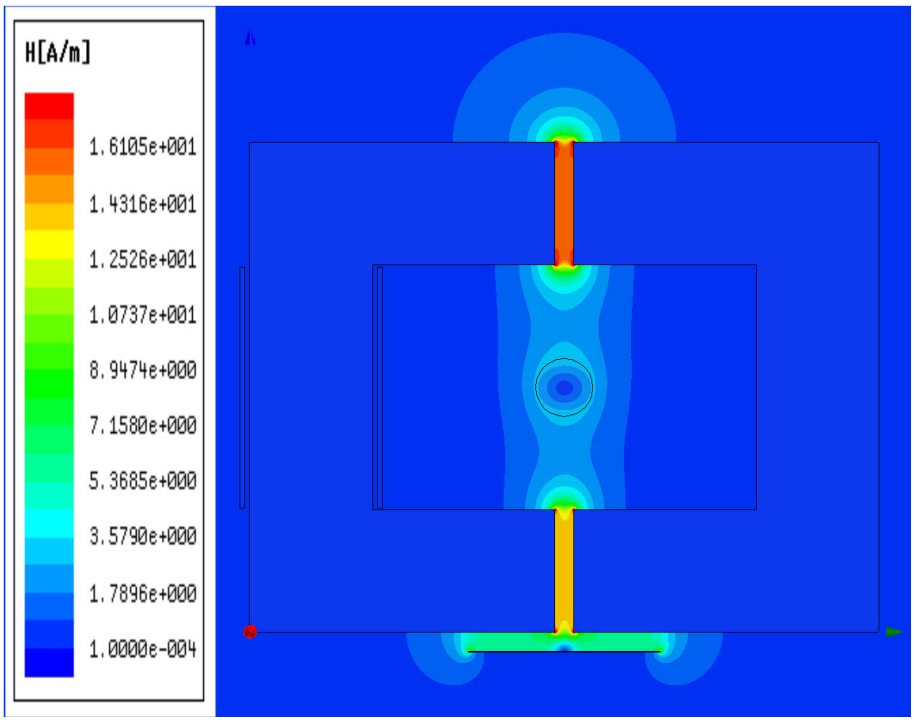

Figure 24: Simulated U-compensation core with strip excitation core. I_{comp} = 0 mA, I_{pri} = 30 mA

The compensation current of 38 mA calculated in Section 5.3.3 induces too much compensation. The magnetic field strength in the lower air gaps is 3.95 A/m when compensated with 38 mA. The right current to compensation the primary current in the simulations is about 29 mA. The error in

calculations is + 27 % so the mean to analyze the problem presented in the earlier chapter is not very accurate.

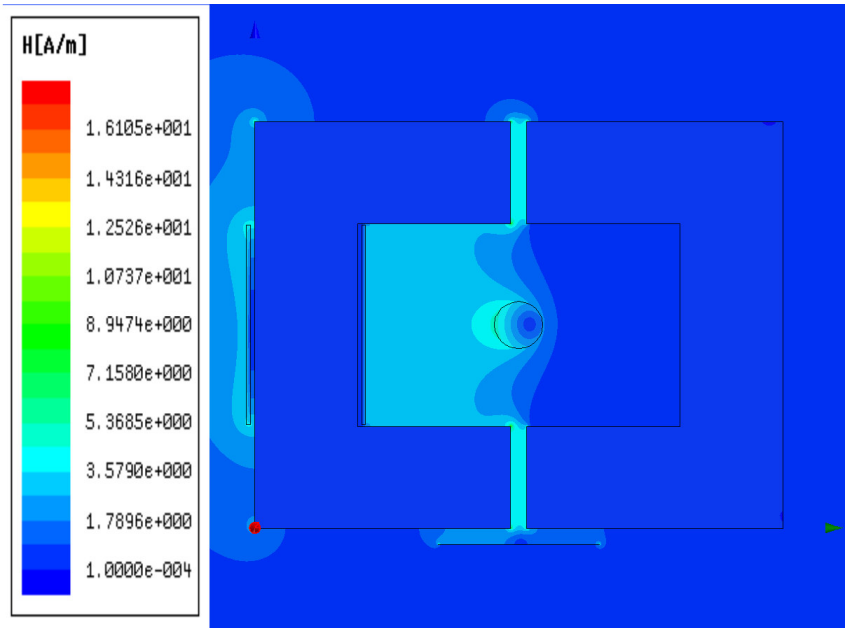

Figure 25: Simulated U-compensation core with strip excitation core. I_{comp} = 38 mA, I_{pri} = 30 mA

5.4.3 Toroidal compensation core with strip excitation core

In the toroid model the conductor carrying the primary current is placed again in the middle of the structure. The current I_{pri} = 30 mA in this conductor is flowing toward the reader. It induces a counter-clockwise magnetic field. A return wire for the current is needed in the simulation model. It is placed far above the model so that it will not interfere with the magnetic fields studied.

Figure 26 shows the simulation result of the magnetic field strength when only 30 mA of primary current flows in the middle conductor. The field strength in the air gaps is 28.97 A/m. The calculated value 29.36 A/m is quite close. The magnetic field strength fringes towards the current conductor. The magnetic field strength is 3.56 A/m at the distance of 3 mm and 8.49 A/m at the distance of 1.0 mm from the air gap.

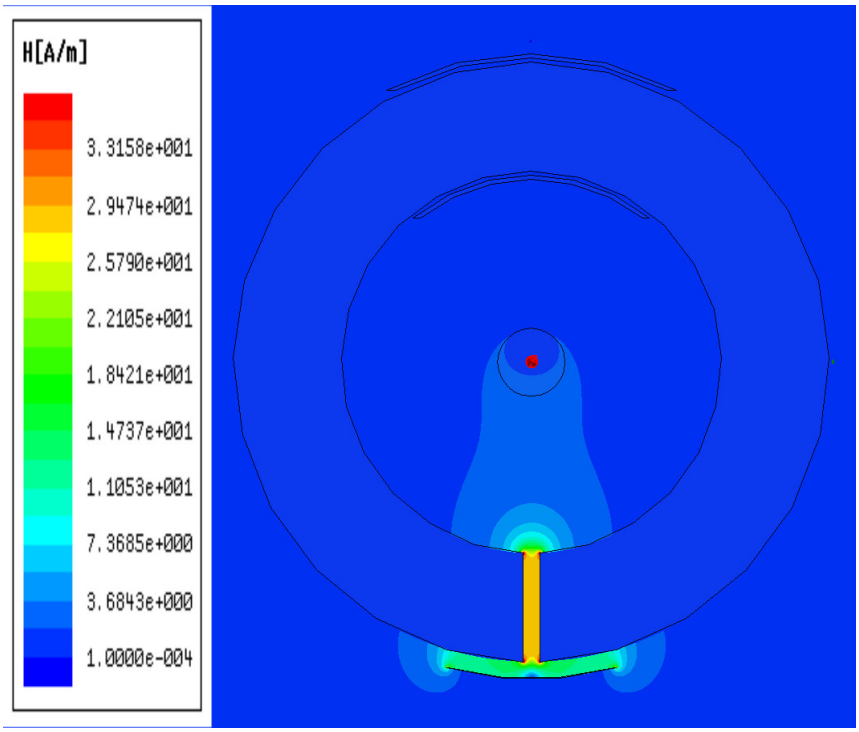

Figure 26: Simulated toroidal compensation core with strip excitation core. Icomp = 0 mA, Ires = 30 mA

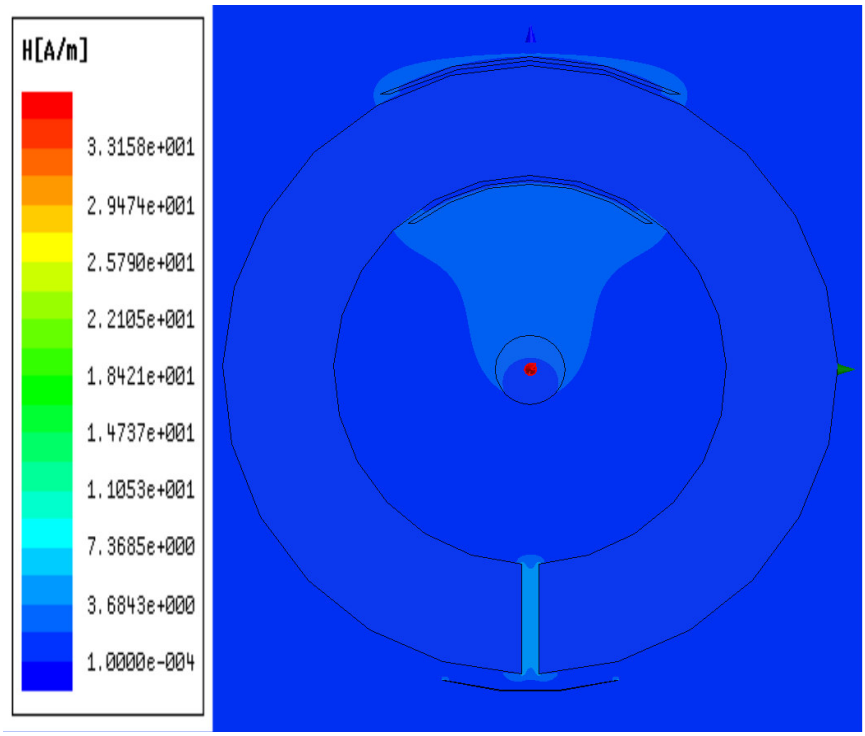

Figure 27: Simulated toroidal compensation core with strip excitation core. I_{comp} = 34 mA, I_{pri} = 30 mA

Figure 27 represents the simulated situation of the primary current compensated. The compensation current in the figure is I_{comp} = 34 mA. There seems to some magnetic field strength left. The magnetic field strength in the air gap is near 4 A/m. Further simulation shows that only 30 mA is needed to compensate the primary current.

5.5 Magnetic circuit concept selection

The numerical simulations revealed practical issues in the designs and the number of concepts could be narrowed down to one. The first option of the U-compensation core with toroidal excitation core had disadvantages with the short cutting magnetic flux. The flow of the flux was difficult to evaluate and the distribution of flux between the two sides of the toroid was uneven and vague. The third option with the toroidal compensation core and strip excitation core seemed to work fine. The problem is in production. The compensation coil would be wound around the toroid. Automatic winding machines for toroids are slow and not many subcontractors have them. The toroid could be manufactured from two half toroids. Such half toroids are however custom parts and quite rarely used. The second option built with U-compensation cores and strip excitation core works fine in simulation. The winding of the compensation coil is easy and can be done with existing winding machines designed for solenoids and such. It could be possible to coil the compensation coil on a hollow plastic tube. The legs of the two U-cores could be then pushed inside so that the air gap would be inside in the middle of the plastic tube. The second option, U-compensation cores and a strip excitation core, was ultimately chosen as the model used in the prototype.

6 Testing Fluxgate prototype sensor

6.1 Testing

The testing of the prototype sensor emphasized studying various excitation cores and coils. Also, the compensation core and coils were studied. It was attempted to find he effects of each part to the whole sensor. Magnetic shielding was tried superficially.

6.1.1 Excitation coil and core

The heart of the device is the excitation coil and core which sense the magnetic field. The excitation core was designed to be 5 mm high, 20 µm thick and 10 mm long. The first excitation coil had 150 turns as suggested in the publication from Vacuumschmelze [31]. These pieces together with the DRV401 created an oscillation frequency of about 150 kHz, which was too low for the IC to work. The excitation probe has to oscillate in a frequency range of 250 kHz to 550 kHz for the IC to work properly. The low frequency oscillation indicates too high inductance of the excitation probe. The inductance can be lowered by reducing the number of coil turns or by adjusting the dimensions or material of the core. It was decided to adjust the dimensions of the core. A smaller core needs less magnetization to be saturated and it saturates more rapidly. The new dimensions of the core were 1 mm high, 20 µm thick and 10 mm long as in *Excitation core 2* contained in Table 3. Furthermore, a new excitation coil with 150 turns was made to better fit the smaller core as in *Excitation coil 1* of Table 3. The new oscillation frequency was 435 kHz. It was quite close to the oscillation frequency (459 kHz) of the excitation probe from Manufacturer B. Three other excitation coils and cores were made after the first test. The properties of these coils and cores are shown in Table 3. These various coils and cores were used in all combinations and the oscillation frequencies are shown in Table 4.

Table 3: Used excitation coils and cores

Excitation coil 1	***Excitation core 1***
150 turns of 0.15 mm wire	1 mm x 5 mm x 20 um
Coil length 10 mm	
Coil cross section 3,6 mm x 1,3 mm	
Excitation coil 2	***Excitation core 2***
150 turns of 0.15 mm wire	1 mm x 10 mm x 20 um
Coil length 7 mm	
Coil cross section 3,6 mm x 1,3 mm	
Excitation coil 3	***Excitation core 3***
100 turns of 0.15 mm wire	2 mm x 10 mm x 20 um
Coil length 10 mm	
Coil cross section 3,6 mm x 1,3 mm	
Excitation coil 4	***Excitation core 4***
200 turns of 0.15 mm wire	2 mm x 10 mm x 40 um
Coil length 10 mm	
Coil cross section 3,6 mm x 1,3 mm	

The driver circuit of DRV401 drives the current through the excitation probe. The direction of the current is switched when the current reaches 28 mA. This switching of the current direction creates the oscillation in the circuit. The results in Table 4 show that an increased number of coil turns lower the oscillation frequency. The oscillation frequency is lowered also by an increase in the dimensions of the core. These results are uniform with the theory in Section 5.3.1. A combination of coil 1 and core 2 were chosen to be the ones used in the tests to come.

Table 4: Frequencies of the combinations

Coil used	**Core used**	**Frequency**		**Coil used**	**Core used**	**Frequency**
Coil 1	Core 1	703 kHz		Coil 3	Core 1	1514 kHz
Coil 1	Core 2	435 kHz		Coil 3	Core 2	758 kHz
Coil 1	Core 3	305 kHz		Coil 3	Core 3	615 kHz
Coil 1	Core 4	202 kHz		Coil 3	Core 4	500 kHz
Coil 1	No core	1056 kHz		Coil 3	No core	1695 kHz
Coil 2	Core 1	460 kHz		Coil 4	Core 1	435 kHz
Coil 2	Core 2	340 kHz		Coil 4	Core 2	292 kHz
Coil 2	Core 3	246 kHz		Coil 4	Core 3	219 kHz
Coil 2	Core 4	160 kHz		Coil 4	Core 4	138 kHz
Coil 2	No core	714 kHz		Coil 4	No core	568 kHz

The excitation cores are made of a soft ferrite material. It is fragile and for better handling the thin stripes are put on a plastic rod. The ready excitation cores can be seen in Figure 28 in the lower right corner. The excitation coils are made so that the excitation cores can be pushed inside the coil and pulled out easily.

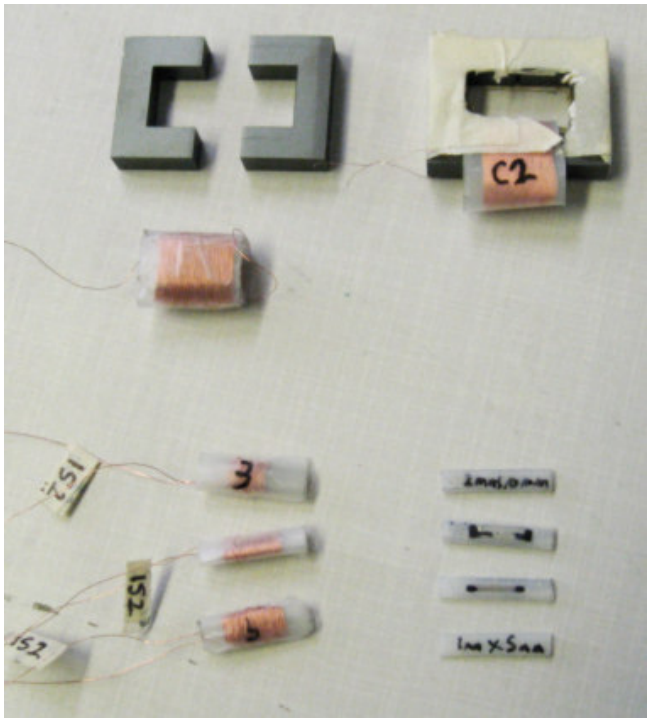

Figure 28: Two compensation cores and coils on top. Excitation coils and cores on bottom

6.1.2 Compensation coil and air gap design

It was decided to build the compensation coil differently to the way it was simulated. The compensation coil should be easily changeable. Therefore, the compensation coil is wound around a hollow body. The coil is then placed around one of the air gaps. The excitation coil is placed inside the compensation coil next to the air gap. Changes in the number of turns were also made. It was decided to increase the number of compensate coil turns to 400. The 400 turns are more than the calculations and simulations estimated. The handmade prototype sensor has more non-idealities than a ready product. The extra turns might be needed to build a working prototype and to compensate a 300 mA current. It is regarded that the extra turns

cause no harm. Various compensation core air gap lengths were also tested. The core material was in all cases the same. The compensation core 4 with a single 1 mm air gap was handmade. The other leg from both U-cores was grinded by 0.5 mm creating a total air gap of 1 mm when pushed together. Table 5 shows the used compensation coil and four cores.

Table 5: Used compensation cores and coils

Compensation core 1	***Compensation coil 1***
2 x 1 mm air gap	400 turns of 0,15 mm wire
	Coil length 17 mm
Compensation core 2	
2 x 0,5 mm air gap	
Compensation core 3	
2 x 0 mm air gap	
Compensation core 4	
1 x 1 mm air gap	

All four compensation cores worked well. They all were able to compensate DC- and AC-current and a combination of these. AC-currents were tested until frequency of 2 kHz. The maximum DC-current that the sensor could compensate with the compensation cores are shown in Table 6.

Table 6: Maximum compensation

Core used	**Max compensation**
Compensation core 1	660 mA
Compensation core 2	630 mA
Compensation core 3	660 mA
Compensation core 4	510 mA

The effective permeability of the compensation core increases as the air gap decreases. This can be seen from Equation (13). Higher effective permeability leads to higher magnetic flux density. At the same time as the air gap decreases also the fringing flux decreases. The excitation coil senses less of the flux induced by the primary current when the fringing flux decreases. These two effects affect the sensitivity of the system and the

amount of primary current that can be compensated and measured. The less the sensor can compensate the more sensitive it is. Table 6 shows that the compensation core 4 makes the system to be the most sensitive. It combines high effective permeability and a large air gap because it has only a single 1 mm air gap. The compensation core 2 is somewhat more sensitive than compensation core 1 but halving the width of the air gap does not make a major difference. The compensation core 3 has no visible air gaps at all. The two U-cores are just pushed together. It seems that the little roughness in the cross areas of the U-cores is enough to create a fringing flux. The sensitivity is about the same as of the compensation core 1.

The driver operating the compensation coil puts only little over 1 mA in the compensation circuit, though it was estimated to be 2 mA in Section 5.3.2. The ~1 mA current flows through the measuring resistor R_4 (620 Ω) and creates 625 mV over the resistor. The differential amplifier reading the resistor has a gain of four. The output of the sensor is driven to either rail when the differential amplifier amplifies the 625 mV to 2.5 V. This 2.5 V is added or subtracted from the zero level of 2.5 V. Thus the output of the sensor is either 0 V or 5 V.

The comparison of the results with the calculations and simulations shows that the number of turns in the tested compensation coil was overestimated. The compensation core 1 would need 182 turns to compensate 300 mA residual current with 1 mA flowing through the compensation coil. Only 91 turns would be needed if the current through the compensation coil was 2 mA as expected. The calculations estimated 190 turns and the simulations 150 turns with 2 mA flowing through the compensation coil.

6.1.3 Magnetic shielding

The prototype sensor was found to be very sensitive to external magnetic fields. Output offset increases and decreases when the sensor is rotated in any axis. The output signal reached easily both supply rails when rotated in

the correct directions without any magnetic shielding. It was first thought that the output signal offset would be caused by the earth's magnetic field. A normal compass, however, showed to random directions when moving it around the laboratory. Sensitivity was tested with a permanent magnet that created a ± 20 mV offset error from a distance of 1.5 m. It was concluded that external magnetic fields were induced by the various machines and current conductors.

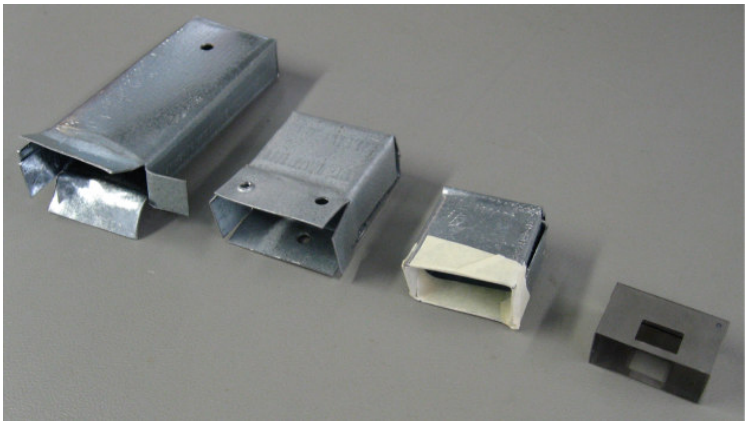

Figure 29: The magnetic shields used

Figure 29 shows the magnetic shields used. The first three from the left are self-made from 1mm thick nickelized steel plate. They all reduced the external magnetic fields coupling to the sensor. The output would drift ± 1 V and it would not reach the supply voltage rails. The 1 V drift is still too high compared to the 300 mV output signal at 80 mA current. The shield pictured on the right is a shield used by Manufacturer B to cover their whole sensor. The DC-offset on the output dropped to 500 mV in the maximum offset position when putting this shield on the magnetic circuit of the prototype sensor. This was the best shield though it did not even cover more than half of the magnetic circuit. The cover used by Manufacturer B is probably manufactured from mu-metal or similar high permeability material. The relative permeability of the mu-metal is in the class of tens of thousands compared to the steel used that has relative permeability of no more than a thousand [25]. Mu-metal would be an effective shielding material also for the

prototype sensor. The sensor of Manufacturer B has no offset error when rotating it around any axis.

6.2 Tolerance analysis

Tolerance analysis provides a view to the measurement accuracy. All the components have a tolerance and their value varies in normal operation within this tolerance. Tolerances have an effect on the final output signal and its error. The critical components can be identified with this analysis and special attention can be taken to choose and design these components. The datasheet of the IC DRV401 lists the possible variations of the parameters. The prototype sensor measures both AC- and DC-currents. The analysis is done by worst case values. For simplicity, the effect of tolerances is calculated in DC-measurement with 1 mA compensation current flowing in the compensation circuit. The handmade magnetic circuit is left out of the scope of this thesis because of its complexity. In the AC-current measurement, the filters of the compensation current are used and the tolerances of the capacitors C_6 and C_5 start to have an effect. The identified critical components and their tolerances are gathered in Table 7.

Table 7: Tolerances and offsets of the critical components

IC differential amplifier	
Offset voltage	± 0.1 mV
Gain error	± 0.3 %
IC compensation loop	
PWM deviation @ 50%	± 0.03 %
IC reference voltage	
2.5V	± 5 mV
Resistors R4-R7	
Value tolerance	± 0.5 %
Resistor R2	
Value tolerance	± 1 %

Equation (31) shows how the output of the sensor depends on the components. R_{osc} = 1 MΩ is the resistance of the oscilloscope and, together

with R_2, it creates a voltage divider. The tolerance of R_2 affects this division of the voltage. The tolerances of $R_4 – R_7$ affect the current flowing through the compensation circuit. The tolerance of R_4 also affects the voltage read by the differential amplifier of the IC. The error in PWM deviation adds to the current in the compensation loop. The change in PWM means a change in current that is measured. The PWM error multiplies the compensation current.

$$
\begin{aligned}
V_{\text{out}} &= \frac{R_{\text{osc}}}{R_{\text{osc}} + R_2}\left(V_{\text{ref}} + G \cdot V_{\text{R4}} = V_{\text{ref}} + G \cdot \left(I_{\text{comp}} \cdot R_4\right)\right) \\
&= \frac{1\text{M}\Omega}{1\text{M}\Omega + 10\text{k}\Omega \cdot (1 \pm 0.01)}\left((2.5\text{V} \pm 5\text{mV}) + 4 \cdot (1 \pm 0.003) \cdot \right. \\
&\left. [620\Omega \cdot (1 \pm 0.005) \cdot 1\text{mA}(1 \pm 0.005) \cdot (1 \pm 0.0003) \pm 0.1\text{mV}]\right)
\end{aligned}
\qquad \textbf{(31)}
$$

$$
\begin{aligned}
&\text{Nom} = 4.931\text{V} \\
&\text{Max} = 4.968\text{V} \\
&\text{Min} = 4.893\text{V}
\end{aligned}
$$

The error resulting from the component tolerances is ± 37 mV. It is about ± 0.8 % of the output voltage of 4.931 V. The real value is higher as the effect of the capacitances is taken into account in the AC-measurements. The magnetic circuit has also tolerances and, as it is handmade with low-tech tools, the tolerances can be quite high. All the tolerances have also a temperature dependent part.

6.3 Failure modes and effects analysis

Failure modes and effects analysis study the results of component and system failures. Failures can be total breakdowns or notable changes in original values. The effects are examined at device level and inverter system level. The severity of the failure is estimated in the range from 0 to 4, where 0 is no harm and 4 is critical harm. The occurrence estimates the possibility of the failure, 1 is low possibility and 4 is high possibility. The criticality of the failure is estimated by multiplying the severity and occurrence of the specific

failure. The higher the value is the more critical the failure is. Appendices 4, 5, and 6 show the complete FMEA table.

6.4 Test results

The prototype sensor that was built works as expected. It is able detect rapid 30 mA changes and it can easily compensate a current of 300 mA. The frequency response is in order. The output signal does not attenuate in the frequency range of DC to 2 kHz. Figure 30 shows the sensor output signal for a 2 kHz, 80 mA current. The setup uses the compensation core 1. The ripple in the output is about 80 mV_{p-p}, the output being 480 mV_{p-p}. It can be decreased by lowering the -3 dB frequency of the output RC-filter. The –3 dB frequency is 66.3 kHz in Figure 30. It is high compared to the maximum measuring frequency of 2 kHz and can easily be lowered. Figure 31 shows some peaking in the measuring output. The integrator in the measuring circuit causes the peaks. The peaks are common for I-type controllers. The increased filtering in sensor output will eliminate these peaks but might round the waveform too much if poorly designed.

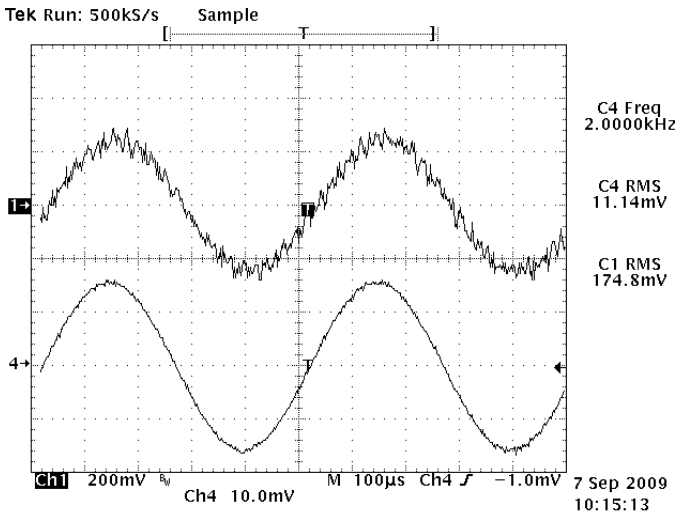

Figure 30: Prototype sensor output for 2 kHz, 80 mA sine current (CH 1 = V_{out} , CH4 = current, 10 mV = 50 mA)

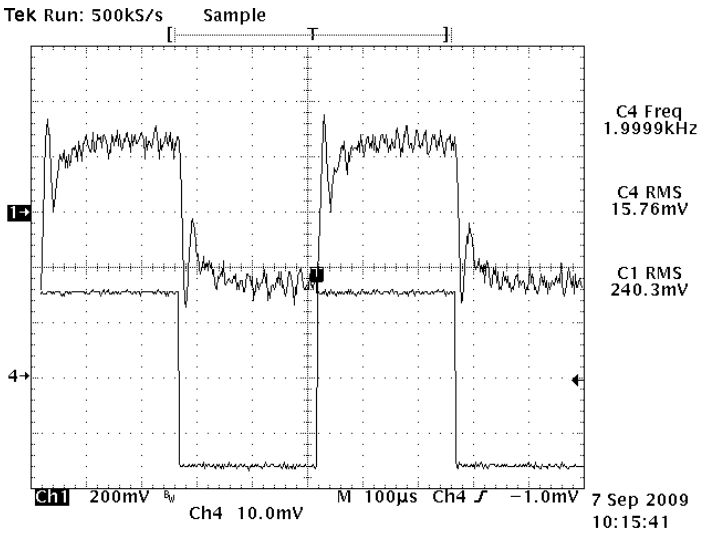

Figure 31: Prototype sensor output for 2 kHz, 80 mA square current (CH 1 = V_{out} , CH4 = current, 10 mV = 50 mA)

7 Summary

The thesis dealt with residual currents in grid feeding photovoltaic systems using transformerless inverters. Inverters with transformers have minimum residual currents because of the galvanic separation between the grid and the solar panels. However, their efficiency is decreased because of the losses in the transformer. The transformer also increases the size and costs of the inverter.

Two commercial residual current sensors were benchmarked. They fulfilled the requirements of the standard VDE DIN 0126-1-1. Sensor A could not measure reliably frequencies between DC and 40 Hz, though it could measure DC. It had a peak in the frequency range. A square waveform was distorted in the output signal at the frequency range. The frequency response of Sensor A increased steadily between 40 Hz and 2 kHz. The change was about 10 %. The compensation of the increasing gain would require a complex external circuit. Sensor B had a constant frequency response between DC and 5 kHz. It had a peak in the frequency response between 5 kHz and 11 kHz. The peak was very temperature sensitive. Both sensors were temperature stable in the important frequency range of DC to 2 kHz excluding frequency range DC – 40 Hz from Sensor A. The output of Sensor B had to be filtered with an RC-filter with a – 3 dB frequency at 4.8 kHz to get a less noisy output signal. Sensor B caused a 70 mV_{p-p} ripple in the + 5 V supply. The ripple was filtered with two 100 nF capacitors parallel in the supply and the ripple decreased to 25 mV_{p-p}. The power consumption of the Sensor A was over 14 times the power consumption of Sensor B. Sensor A used only 1.14 watts.

Hall sensors and flux gate sensors were identified to be cost efficient and effective in residual current measurements. However, the studies showed that hall sensors are not sensitive enough to be used in residual current measurements. Their sensitivity is only about 1 mV/mT. Furthermore, Hall sensors have quite high offset voltages. Fluxgate technology can measure

currents of tens of milliamperes. The sensitivity of the sensors is hundreds of mV/mT. The disadvantage of the fluxgate sensors is their higher purchase price when compared to the Hall sensors.

The residual current is caused by the ground capacitance between the solar cells and their grounded frame. A voltage is created over this capacitance and the current through the ground capacitance depends on the frequency and the amplitude of the voltage. The residual current is common mode. The ground capacitance depends on the solar panel type used and on the weather conditions. Crystalline silicon cells have typically capacitances from 50 to 150 nF/kW_p. Humidity can increase the residual currents by tens of times. The voltage depends on the modulation method and topology used in the inverter. The modulation method is the dominant factor in residual currents. Typical methods are bipolar and unipolar modulation. Bipolar modulation creates a low frequency voltage over the ground capacitance and the residual currents are minimal. Unipolar modulation creates a high frequency voltage component over the ground capacitance which increases the residual current. The effects of residual currents are higher system losses, increased solar panel degradation and EMI problems. The residual currents also cause fire hazard and electric shock hazard.

The prototype sensor built during this thesis investigation was based on the fluxgate technology. The sensor used IC DRV401. The compensation core was built of two U-cores having two 1 mm air gaps. The compensation coil had 400 turns. The excitation core was made of a Vitrovac 6025Z strip and the excitation coil had 150 turns. The sensor could easily measure currents of 300 mA and rapid changes of 30 mA could be detected instantly. The frequency range from DC to 2 kHz could be measured. The output of the sensor was very noisy but it was filtered with a lowpass filter. The prototype sensor was noted to be sensitive to external magnetic fields. The sensor should be shielded with a high permeability cover. Future study of the sensor should focus on the magnetic shielding of the sensor and design of the magnetic circuit.

References

[1] Solarbuzz, 2009. World PV industry report summary [Online document]. [quoted 23.6.2009].
Available: http://www.solarbuzz.com/Marketbuzz2009-intro.htm

[2] M. Calais, V. G. Agelidis and M. Meinhardt, 1999. Multilevel converters for single-phase grid connected photovoltaic systems: An overview. Solar Energy, Vol. 66, No. 5, pp. 325-335, 1999.

[3] Honeywell Solid State Electronics Center, 2000. Magnetic Current Sensing. Application Note 209 [Online document]. [quated 25.06.2009].
Available: http://www.ssec.honeywell.com

[4] J.M.A. Myrzik and M. Calais, 2003. String and module integrated inverters for single-phase grid connected photovoltaic systems – a review. Power Tech Conference, Vol. 2, 2003.

[5] B. Marion, et al., 1988. Design and operation of grid-interactive thin-film silicon PV systems. Photovoltaic Specialists Conference, Vol. 2, pp. 1027-1034, 1988.

[6] C.R. Osterwald, T.J. McMahon and J.A. del Cueto, 2003. Electrochemical Corrosion of SnO2:F Transparent Conducting Layers in Thin Film Photovoltaic Modules. Solar Energy Materials & Solar Cells, Vol. 79, pp. 21-33, NREL Report No. JA-520-31724.

[7] R. Gonzalez, et al., 2006. High-Efficiency Transformerless Single-phase Photovoltaic Inverter. Power Electronics and Motion Control Conference, 12th international, pp. 1895-1900, 2006.

[8] O. Lopez, et al., 2007. Eliminating ground current in a transformerless photovoltaic application. Power Engineering Society General Meeting 2007, pp. 1-5, 2007.

[9] J.A. Suul, K. Uhlen and T. Undeland, 2008. Grid Connected Converters for Photovoltaic, State of the Art, Ideas for Improvement of Transformerless Inverters. NORPIE Conference, 9 – 11 June 2008.

[10] E. Gubia, et al., 2007. Ground currents in single-phase transformerless photovoltaic systems. Progress in Photovoltaics: Research and Applications, Vol. 15, pp. 629-650, 2007.

[11] J.M.A. Myrzik and M. Calais, 2003. String and module integrated inverters for single-phase grid connected photovoltaic systems – a review. Power Tech Conference, Vol. 2, 2003.

[12] DIN VDE 0126-1-1, 2006. Selbsttätige Schaltstelle zwischen einer netzparallelen Eigenerzeugungsanlage und dem öffentlichen Niederspannungsnetz. Deutsche Kommission Elektrotechnik, Elektronik Informationstechnik im DIN und VDE. 2006.

[13] Zetex Semiconductors, 2008. Current measurement applications handbook. Application Note 39, Issue 5 [Online document] [quoted 1.9,2009] Available: http://www.zetex.com

[14] R.S. Popovic, J.A. Flanagan and P.A. Besse, 1996. The future of magnetic sensors. Sensors and Actuators, Vol. 56, Issues 1-2, pp. 39-55, 1996.

[15] Honeywell, 1998. A New Perspective on Magnetic Field Sensing. Technical Articles [Online document]. [quoted 11.10.2009]. Available: http://www.ssec.honeywell.com

[16] G. Diemel, et al., 1997. Smart sensor system application: an integrated compass. European Design and Test Conference 1997, pp. 195-199, 1997.

[17] P. Ripka, 2003. Advances in fluxgate sensors. Sensors and Actuators, Vol. 106, Issues 1-3, pp. 8-14, 2003.

[18] P. Ripka and M. Janosek, 2008. Advances in Magnetic Sensors. Sensors, pp. 1-4, 2008.

[19] Texas Instruments, 2009. DRV401 Datasheet [Online document] [quoted 11.10.2009] Available: http://focus.ti.com/lit/ds/symlink/drv401.pdf

[20] Vacuumschmelze, 2007. Application Hints for DI-Current Sensors with the IC DRV401. [Online document] [quoted 11.10.2009] Available: http://www.vacuumschmelze.de/

[21] S. Maniktala, 2004, Switching Power Supply Design & Optimization, McGraw-Hill, ISBN 0-07-143483-6

[22] E.C. Snelling, 1988, Soft Ferrites Properties and applications, Butterworths, ISBN 0-408-02760-6

[23] A. Arkkio, 2009. Design of Electrical Machines. Lecture slides, Lecture 3, spring 2009. Helsinki University of Technology, 2009. [Online Document] [quoted 20.9.2009] Available: https://noppa.tkk.fi/noppa/kurssi/s-17.3030/luennot/lecture_3.pdf

[24] Ferroxcube, 2008. U25/16/6 Datasheet [Online document] [quoted 16.9.2009] Available: http://www.ferroxcube.com/

[25] Wikipedia, 2009. Permeability (electromagnetism) [Website] [quoted 1.10.2009] Available: http://en.wikipedia.org/wiki/Permeability_%28electromagnetism%29

[26] Wikipedia, 2009. Grid tie inverter [Website] [quoted 21.9.2009] Available: http://en.wikipedia.org/wiki/Grid_tie_inverter

[27] I. Lindell and A. Sihvola, 2007. Sähkömagneettinen kenttäteoria: 1. Staattiset kentät 6th ed. Helsinki, Hakapaino Oy. 225 p. ISBN 978-951-672-354-2

[28] Vacuumschmelze, 2007. Tape-Wound Cores for Magnetic Amplifier Chokes VITROVAC 6025 Z. [Online document] [quoted 9.8.2009] Available: http://www.vacuumschmelze.de/

[29] A. Luque and S. Hegedus, 2003. Handbook of photovoltaic science and engineering. West Sussex, John Wiley & Sons Ltd. 1117 p. ISBN 978-0-471-49196-5.

[30] G.P. Willeke, 2008. Progress in industrial crystalline silicon solar PV technology. Photovoltaic Specialists Conference 2008, pp. 1-4, 2008.

[31] Vacuumschmelze, 2007. Closed Loop Current Sensors with Magnetic Probe. [Online document] [quoted 1.10.2009] Available: http://www.vacuumschmelze.de/

[32] H.D. Young and R.A. Freedman 2000. University Physics 10th ed., with modern physics. Addison Wesley Longman Inc. 1027 p. ISBN 0.201-60336-5

[33] D. Gignoux and M. Schlenker, 2002. Magnetism: II – Materials & Applications. Kluwer Academic Publishers, 517 p. ISBN 1-40207-223-6

[34] U.A. Bakshi and V.U. Bakshi, 2008. Basic Electrical Engineering, 1st ed. Pune, India, Technical Publications Pune, 617 p. ISBN 978-8-18431-488-5

[35] A. Bossche and V. Valchev, 2005. Inductors and tranformers for power electronics. Florida, Taylor & Francis Group, 435 p. ISBN 978-1-57444-679-1

[36] N.G. Dhere, V.V. Hadagali and S.M. Bet, 2004. Leakage Current Pathways, Magnitudes And Their Correlation To Humidity And Temperature In High Voltage Biased Thin Film PV Modules. 19th European Photovoltaic Solar Energy Conference, pp. 2170-2173, 2004.

[37] S.V. Araujo, P. Zacharias and B. Sahan, 2008. Novel grid-connected non-isolated converters for photovoltaic systems with grounded generator. Power Electronics specialists Conference, pp. 58-65, 2008.

[38] O. Lopez et al., 2007. Eliminating ground current in a transformerless photovoltaic application. Power Engineering Society General Meeting 2007, pp 1-5, 2007.

[39] O. Lopez et al., 2007. Leakage current evaluation of a single-phase transformerless PV inverter connected to the grid. Applied Power Electronics Conference, pp.907-912, 2007.

[40] IEC 60755 , 2008. General requirements for residual current operated protective devices. The International Electrotechnical Commission, 2008.

[41] IEC 62109-2, 2005. Safety of power converters for use in photovoltaic power systems - Particular requirements for inverters. The International Electrotechnical Commission, 2005.

[42] UL508C, 2002. Power Conversion Equipment. Underwriters Laboratories Inc. 2002

[43] Fraunhofer institute Solare Energiesysteme, 2009. World Record: 41.1% efficiency reached for multi-junction solar cells at Fraunhofer ISE [Online document] [quoted 20.10.2009] Available http://www.ise.fraunhofer.de/

Appendix 1

Schematic for the Flux Gate prototype sensor

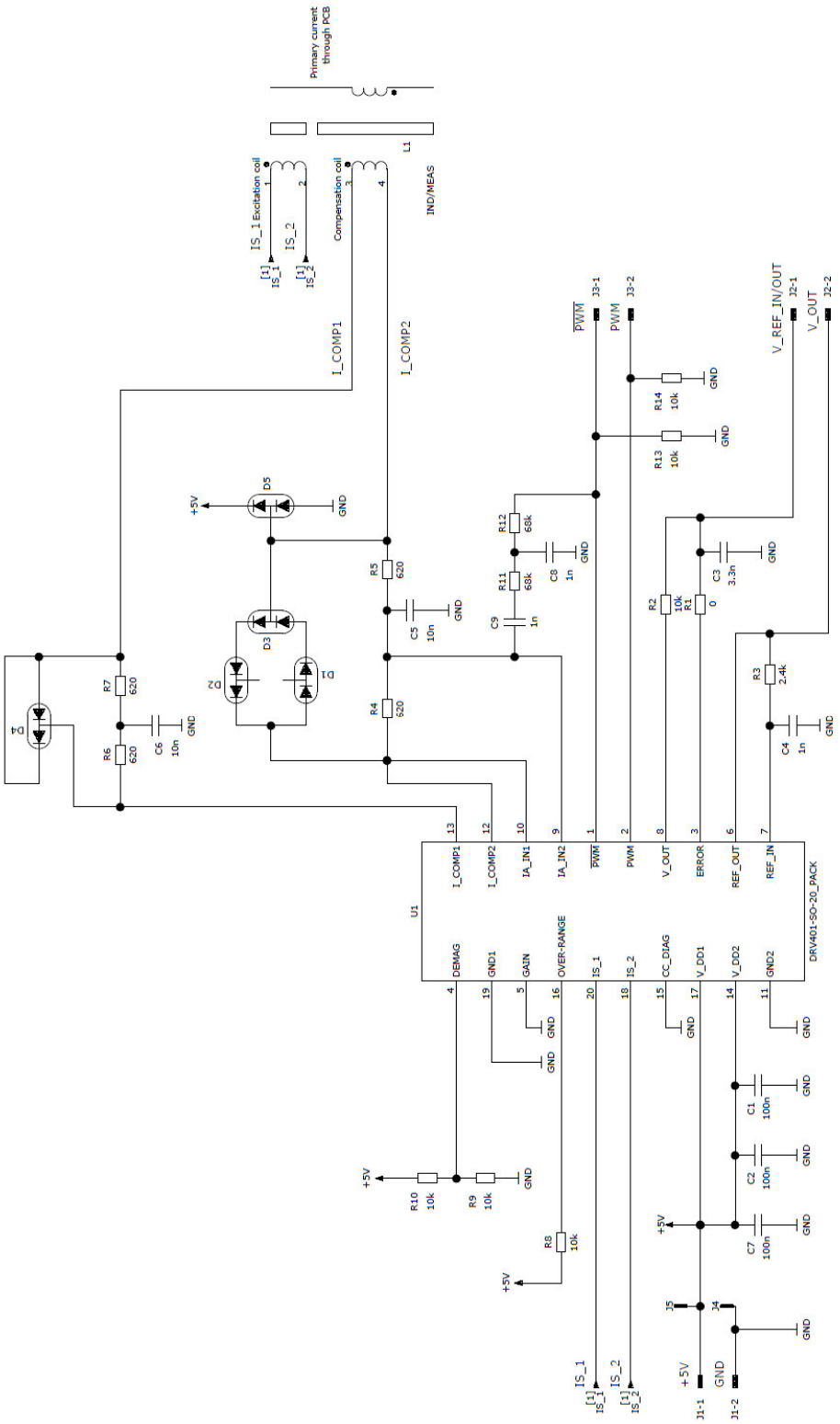

Appendix 2

Bill of Materials for the Flux Gate prototype sensor

Part number	Quantity	Part description	Value	Rating 1	Rating 2	Package	Manufacure
C1	1	Ceramic Chip Capacitor	100n	25V	X7R, 20%	1206	Any
C2	1	Ceramic Chip Capacitor	100n	25V	X7R, 20%	1206	Any
C7	1	Ceramic Chip Capacitor	100n	25V	X7R, 20%	1206	Any
C3	1	Ceramic Chip Capacitor	3.3n	25V	X7R, 20%	1206	Any
C5	1	Ceramic Chip Capacitor	10n	25V	X7R, 20%	1206	Any
C6	1	Ceramic Chip Capacitor	10n	25V	X7R, 20%	1206	Any
C4	1	Ceramic Chip Capacitor	1n	25V	X7R, 20%	1206	Any
C8	1	Ceramic Chip Capacitor	1n	25V	X7R, 20%	1206	Any
C9	1	Ceramic Chip Capacitor	1n	25V	X7R, 20%	1206	Any
D1	1	High-speed Double Diode BAV99	75V	125mA	250mW, 4ns	SOT23	Any
D2	1	High-speed Double Diode BAV99	75V	125mA	250mW, 4ns	SOT23	Any
D3	1	High-speed Double Diode BAV99	75V	125mA	250mW, 4ns	SOT23	Any
D4	1	High-speed Double Diode BAV99	75V	125mA	250mW, 4ns	SOT23	Any
D5	1	High-speed Double Diode BAV99	75V	125mA	250mW, 4ns	SOT23	Any
J1	1	2-pin. Screw connector	250V	13.5A	2 pins		Any
J2	1	2-pin. Screw connector	250V	13.5A	2 pins		Any
J3	1	2-pin pin header			2 pins	P2.54	Any
J4	1	Measuring Pin					Any
J5	1	Measuring Pin					Any
L1	1	Proto measuring transformer					
R1	1	Chip Resistor	0	0.25W, 5%	200V	1206	Any
R3	1	Chip Resistor	2.4k	0.25W, 1%	200V	1206	Any
R4	1	Chip Resistor	620	0.25W, 0.5%	200V	1206	Any
R5	1	Chip Resistor	620	0.25W, 0.5%	200V	1206	Any
R6	1	Chip Resistor	620	0.25W, 0.5%	200V	1206	Any
R7	1	Chip Resistor	620	0.25W, 0.5%	200V	1206	Any
R2	1	Chip Resistor	10k	0.25W, 1%	200V	1206	Any
R8	1	Chip Resistor	10k	0.25W, 1%	200V	1206	Any
R9	1	Chip Resistor	10k	0.25W, 1%	200V	1206	Any
R10	1	Chip Resistor	10k	0.25W, 1%	200V	1206	Any
R13	1	Chip Resistor	10k	0.25W, 1%	200V	1206	Any
R14	1	Chip Resistor	10k	0.25W, 1%	200V	1206	Any
R11	1	Chip Resistor	68k	0.25W, 1%	200V	1206	Any
R12	1	Chip Resistor	68k	0.25W, 1%	200V	1206	Any
U1	1	Sensor signal conditioning IC for Closed-loop magnetic current sensor				SO-20	Texas Inst.

Appendix 3

Layout of the fluxgate prototype sensor

Top side

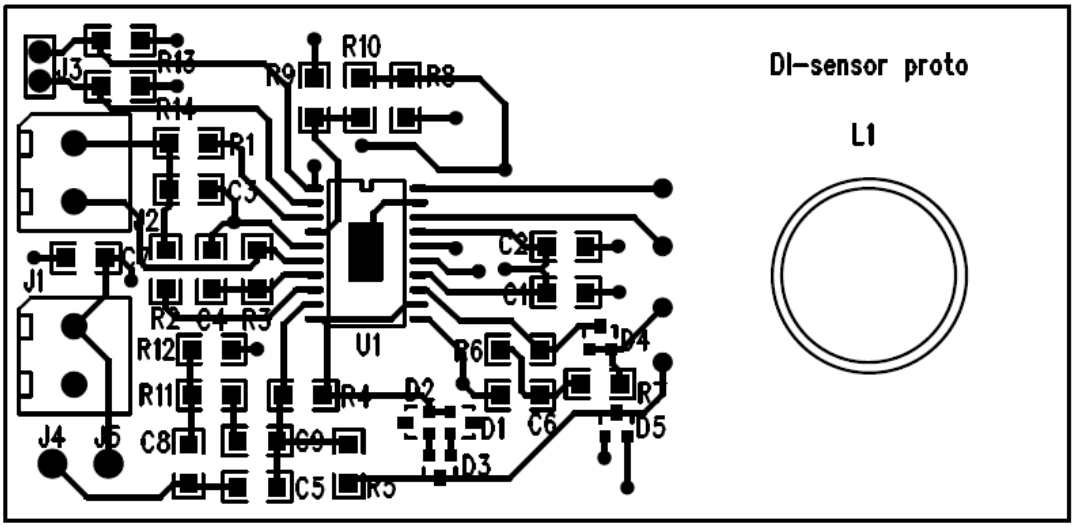

Bottom side

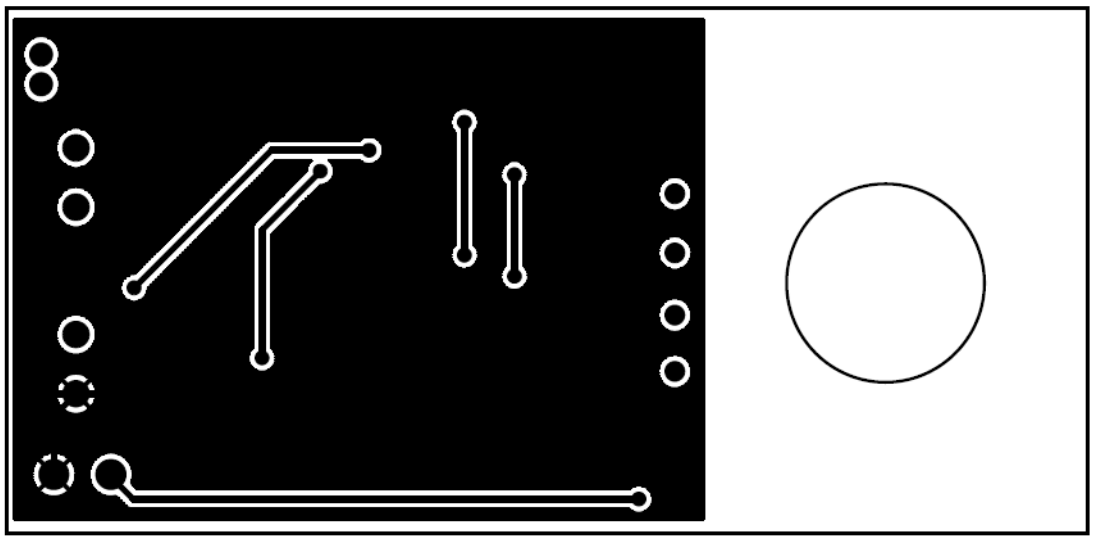

Appendix 4

FMEA 1/3

	A	B	C	D	E	F	G	H	I
1	Component	Component Function	Failure	Failure mode	Device effects	System effects	Severity	Occurrence	Criticality
2	C1	Supply filter for IC	Value decreases	Unstable supply voltage	Random errors in IC	Unreliable measurement	2	1	2
3	C2	Supply filter for IC	Value decreases	Unstable supply voltage	Random errors in IC	Unreliable measurement	2	1	2
4	C3	Output signal filter	Value decreases	Higher ripple passing through	More noise in output	Unreliable measurement	2	1	2
5	C4	Reference voltage filter	Value decreases	Unstable reference voltage	Unstable zero level for ouput	Unreliable measurement	1	1	1
6	C5	Compensation current filter	Value decreases	Higher ripple passing through	More noise in output	Unreliable measurement	2	1	2
7	C6	Compensation current filter	Value decreases	Higher ripple to output	More noise in output	Unreliable measurement	2	1	2
8	C7	Supply filter for board	Value decreases	Unstable supply voltage	Random errors in IC	Unreliable measurement	1	1	1
9	C8	Not assembled							
10	C9	Not assembled							
11									
12	D1	Compensation circuit over voltage protection	breaks to open circuit	Over voltage goes through filter	Filter components degrade	Unreliable measurement and spikes in output	2	1	2
13	D2	Compensation circuit over voltage protection	breaks to open circuit	Over voltage goes through filter	Filter components degrade	Unreliable measurement and spikes in output	2	1	2

Appendix 5

FMEA 2/3

Component	Component Function	Failure	Failure mode	Device effects	System effects	Severity	Occurrence	Criticality
D3	Compensation circuit over voltage protection	breaks to open circuit	Over voltage goes through filter	Filter components degrade	Unreliable measurement and spikes in output	2	1	2
D4	Compensation circuit over voltage protection	breaks to open circuit	Over voltage goes through filter	Filter components degrade	Unreliable measurement and spikes in output	2	1	2
D5	Compensation circuit over voltage protection	breaks to open circuit	Over voltage goes through filter	Filter components degrade	Unreliable measurement and spikes in output	2	1	2
J1	Power connector	breaks to open circuit	No power supplied to device	Device shutdown	No measurent result	4	1	4
J2	V_out and V_ref in/out	breaks to open circuit	No output signal to system	No output signal to system	No measurent result	4	1	4
J3	Not assembled							
J4	Not assembled							
J5	Not assembled							
L1	Compensation coil and excitation coil	Wire break	Open compensation current loop	Error and no output signal	No measurent result	4	1	4
R1	Output pull down in errors	Value increases	Output not pulled down efficiently in errors	Output not presenting the real value in erros	Unreliable measurement	2	1	2
R2	Output signal filter	Value increases	More voltage over the resistor	Lowered measurent result	Permanently changed measurement result	3	1	3

Appendix 6

FMEA 3/3

	Component	Component Function	Failure	Failure mode	Device effects	System effects	Severity	Occurrence	Criticality
31									
32	**R3**	Filtering ref. Voltage, external reference	Value increases	Unstable reference voltage	Unstable zero level for ouput	Unreliable measurement	2	1	2
33	**R4**	Compensation current filter	Value increases	Less compensation current and higher readings for dif.amp.	Max measurement limit decreases	Permanently changed measurement result	3	2	6
34	**R5**	Compensation current filter	Value increases	Less compensation current	Max measurement limit decreases	Permanently changed measurement result	3	2	6
35	**R6**	Compensation current filter	Value increases	Less compensation current	Max measurement limit decreases	Permanently changed measurement result	3	2	6
36	**R7**	Compensation current filter	Value increases	Less compensation current	Max measurement limit decreases	Permanently changed measurement result	3	2	6
37	**R8**	Feature not used							
38	**R9**	Pulling DEMAG-pin low	Value increases	Demag-pin flouting	Demagnetization at startup	Nothing	0	0	0
39	**R10**	Not assembled							
40	**R11**	Not assembled							
41	**R12**	Not assembled							
42	**R13**	Not assembled							
43	**R14**	Not assembled							
44									
45	**U1**	The main IC operating everything	Many possible failures	No operation or changed values	No operation or unreliable measurement	No or unreliable measurement	4	2	8